Structure of the manganese intermediates of photosynthetic oxygen evolving complex revealed by PELDOR

パルス電子-電子二重共鳴(PELDOR)法を用いた光合成酸素発生系 Mn 中間体の構造解析

Doctoral dissertation

Mizue Asada

浅田　瑞枝

Contents

Abbreviations

EPR: electron paramagnetic resonance

PELDOR: pulsed electron-electron double resonance

ESE: electron spin echo

ESEEM: electron spin-echo envelope modulation

ENDOR: electron-nuclear double resonance

DFT: density functional theory

XAS: X-ray absorption spectroscopy

EXAFS: Extended X-ray absorption fine structure

CW: continuous wave

Mes: 2-morpholinoethasulfonic acid

EDTA: Ethylenediaminetetraacetic acid

Tris: tris(hydroxymethyl)aminomethane

PS II: photosystem II

OEC: oxygen-evolving complex

YD: Tyr161 for higher plants and Tyr160 for cyanobacteria of the D2 subunit in PS II

YZ: Tyr161 of the D1 subunit in PS II

ZFS: zero-field splitting

General Background

Oxygen is an essential molecule for breathing creatures on earth. Production of O_2 by photosynthesis has provided the lush environment of the earth since 2.7 billion years ago when cyanobacteria started photo-oxidation of water, growing the diversity of lives. The earth's rich natural environment has been supported by the photosynthetic oxygen evolution [1-3].

Photosynthesis is a light energy transforming reaction. Using the light energy, carbohydrate and ATP are produced from oxidation of water and reduction of carbon dioxide, and during this synthetic process O_2 molecules are released as a by-product of water oxidation. A series of light-dependent reactions in photosynthetic reaction center proteins begins with oxidation of water molecules in photosystem II and ends in hydrogenation of NADP in photosystem I. In photosystem II, the light energy is caught by the antenna proteins, light harvesting complexes (LHC) around PS II core complex, and the harvested energy is transferred through several pigments to the special pair chlorophyll (P680). Upon charge separation in P680, one electron is released and transferred through pheophytin (Pheo) and quinone A (Q_A) to quinone B (Q_B). The reduced Q_B molecule is released into the membrane lipid bilayer and donates one electron to Photosystem I via Cyt b_6f complex. NADPH reduced in Photosystem I is used to produce carbohydrate (depicted in Figure G-1).

The molecular structure of photosystem II (PS II) isolated from cyanobacteria *Thermosynechococcus vulcanus* has been clarified by X-ray crystallography. PS II contains homologous D1 and D2 reaction center proteins and antenna proteins CP43

and CP47 for the core complex, and have several extrinsic proteins as illustrated in Figure G-2. The inner membrane subunits D1 and D2 face to each other and arranged symmetrically around the pseudo C_2 axis. Antenna complex LHC II is located around the outside of the core complexes. Cyt b_{559} is attached between D1/D2 and CP43 subunits [2, 3].

The structure of PS II core complex is highly conserved in various photosynthetic species, whereas the number and kind of extrinsic subunits differs depending on the photosynthesis species. PS II complex in cyanobacteria has PsbO, PsbU, PsbV on the lumenal side of PS II, whereas the PS II complex in higher plants contains PsbP and PsbQ instead of PsbU and PsbV [4, 5]. The PsbO stabilizes the structure of oxygen-evolving complex and is necessary for O_2 evolution. The presence of extrinsic subunits enhances the Ca^{2+} and Cl^- affinity and the O_2 activity.

Light-induced electron transfer occurs in PS II (Figure G-3). The oxidized P680 is reduced by oxidizing the tyrosine Y_Z in D1 subunit and returns to the initial state. Oxidized Y_Z oxidizes the Mn cluster located in the lumenal side of PS II, the direct catalyst of the water oxidation. There is another redox active tyrosine residue in the D2 subunit, Y_D, which is located symmetrically to that of Y_Z in D1 subunit. $Y_D^{\bullet}$ is not in the main electron transfer pathway, but is oxidized by P680 after illumination and get to be a stable radical for EPR measurement. The stable $Y_D^{\bullet}$ radical has been a benchmark in determining the relative position of the radical molecules and the Mn metals in PS II.

The Mn cluster in PS II is a catalytic site of water oxidation, where cofactors 4 Mn and 1 Ca ions are connected by oxo bridges in a boxy structure. The Mn cluster and the surrounding amino acids are called the oxygen-evolving complex (OEC). To date, to determine the structure of the Mn cluster has been a major problem for deep understanding of the water oxidation process in PS II. The OEC structure has been analyzed by various techniques including visible, UV, and X-ray spectroscopic measurements, EPR and X-ray crystallography. Previous X-ray crystallographic analyses have determined the molecular structure of PS II at resolutions of 2.9-3.8 Å [6-8]. These results provided significant information on the overall structure of PS II including the locations of various subunits and cofactors of OEC. However, the detailed structure of the Mn_4Ca cluster (i.e. the positions of 4 Mn atoms and 1 Ca atom and the oxo-bridges between them) has not been revealed. Extended X-ray absorption fine structure (EXAFS) and polarized EXAFS have been utilized to examine various models proposed for the structure of the OEC, including the information as to the distances between Mn-Mn and Mn-Ca pairs [9-13]. Some of the EXAFS models have given similar structures as that revealed by the crystallographic studies [14, 15], however, the structure of the OEC has remained to be an unresolved problem. This situation was greatly improved by the recent crystallographic analysis of PS II at a resolution of 1.9 Å [16]. The X-ray study revealed the locations of the individual Mn and Ca ions as well as the presence of the five O atoms connecting the metal ions. All of the amino acids ligated to the metal cluster were identified and it was clarified that each Mn ion has six-coordination and the Ca ion has seven-coordination. A more recent study with X-ray free-electron laser (XFEL) secured the molecular structure of the Mn cluster without damage by the X-ray illumination [17].

The Mn_4CaO_5 cluster forms a distorted chair with the three Mn atoms (labeled Mn1-Mn3) and the Ca atom connected by four oxygen atoms (O1-3, 5) to organize a distorted cubic form, and the fourth Mn (Mn4) and the last oxygen (O4) connected outside of the cube (Figure G-4). It also revealed the presence of the four water molecules, i.e., two of them are ligated to Ca and the other two water molecules are ligated to Mn4 in the Mn cluster. The four Mn ions labeled as Mn1-4 and the Ca ion are connected by five oxygen atoms. The amino acids ligated to these Mn atoms are; His 332, Asp342 and Glu189 ligated to Mn1, Asp342, Ala344 and D2-Glu354 ligated to Mn2, Glu333 and D2-Glu354 ligated to Mn3, Glu333 and Asp170 ligated to Mn4 [17].

The X-ray crystallographic studies have revealed the structure of PS II core complex isolated from *Thermosynechococcus* including the structure of the OEC [16, 17]. However, the structure of the stable state is currently available, and many researches are still challenging to determine the structures of reaction intermediates occurring during water oxidation. The assembly process of the Mn cluster is also undetermined. The molecular and electro-magnetic structure of the intermediates will provide detailed information as to the dynamic structural changes and the electron transfer process in PS II.

EPR spectroscopy is a well-established method to detect electron spins of molecules and magnetic structures of transition metals, and has been applied to clarify the structure of the Mn cluster in PS II. An unpaired electron resonates with microwave under the following condition:

$$h\nu = g\mu_B H \qquad (1)$$

where *h* is Planck constant, ν is the microwave frequency, *g* is the effective *g*-factor (*g* = 2 for the free electron), μ_B is the magnitude of Bohr magneton and *H* is the strength of the applied magnetic field. For measuring ESR signals, the microwave frequency is fixed and the strength of the external magnetic field is swept. EPR signals provide the information on the effective g-factor, which varies depending on the environment of the electron spin. Spin Hamiltonian for one electron spin is written as follows:

$$\mathcal{H} = \mu_B \boldsymbol{H} \cdot \boldsymbol{g_e} \cdot \boldsymbol{S} + \mu_N \boldsymbol{H} \cdot \boldsymbol{g_N} \cdot \boldsymbol{I} + \boldsymbol{S} \cdot \boldsymbol{D} \cdot \boldsymbol{S} + \boldsymbol{S} \cdot \boldsymbol{A} \cdot \boldsymbol{I} + \boldsymbol{I} \cdot \boldsymbol{Q} \cdot \boldsymbol{I} \qquad (2)$$

where $\boldsymbol{H}$ is the external magnetic field vector, $\boldsymbol{g_e}$ and $\boldsymbol{g_N}$ are the *g*-tensors of electron and nuclear, respectively; $\boldsymbol{S}$ and $\boldsymbol{I}$ are the spin operators for electron and nuclear, respectively, $\boldsymbol{\mu_N}$ is the nuclear magneton, and $\boldsymbol{D}$ is the fine structure tensor, $\boldsymbol{A}$ is the hyperfine tensor, and $\boldsymbol{Q}$ is the nuclear quadrupole interaction tensor. For two electron spins, spin Hamiltonian is written as:

$$\mathcal{H} = \mu_B \boldsymbol{H} \cdot \boldsymbol{g_{e1}} \cdot \boldsymbol{S_1} + \mu_B \boldsymbol{H} \cdot \boldsymbol{g_{e2}} \cdot \boldsymbol{S_2} + \boldsymbol{S_1} \cdot \boldsymbol{D_{ee}} \cdot \boldsymbol{S_2} + \boldsymbol{S_1} \cdot \boldsymbol{J_{ee}} \cdot \boldsymbol{S_2} \qquad (3)$$

where $\boldsymbol{g_{ei}}$ is the *g*-tensor for *i*-th spin, $\boldsymbol{S_i}$ is the spin operator for *i*-th spin, $\boldsymbol{D_{ee}}$ is tensor for the dipole, and $\boldsymbol{J_{ee}}$ is the exchange interaction between two spins. The shape of an EPR spectrum is dependent on the *g*-tensor, which is influenced by the structure around electron spins (e.g. hyperfine structure caused by electron-nuclear interaction, fine structure caused by electron-electron interaction and binding ligands, *g*-factor and nuclear quadrupole interaction). Thus these parameters are adjusted to analyze the EPR signals.

An EPR spectrum recorded for a protein sample consists of inhomogeneous lines because of inhomogeneous local magnetic field originating from the nearby electron and nuclear spins. Pulsed EPR is a useful method to isolate the contributions from the

intermolecular structure such as the dipole interactions. In pulsed EPR measurements, the spin is nutated by applied microwave pulses. The time evolution of spin nutation is expressed as unitary operators:

$$U_{tp} = \exp(-i\mathcal{H}_p t_p/\hbar) \ , \quad U_{tn} = \exp(-i\mathcal{H}_n t_n/\hbar) \qquad (4)$$

where t_{tp} is the pulse length, t_n is the time interval between microwave pulses, and $\mathcal{H}_p$ and $\mathcal{H}_n$ are spin Hamiltonian during and without microwave pulses. Standard spin echo signal is measured using $\pi/2$-τ-π pulse sequence described in Figure G-5. The density matrix operator σ of the electron spin at the time of $t_\pi+\tau+t_\pi+t$ is written as:

$$\sigma\left(t_{\pi/2}+\tau+t_\pi+t\right) = U_{t_{\pi/2}+\tau+t_\pi+t} \cdot \sigma_0 \cdot U^*_{t_{\pi/2}+\tau+t_\pi+t} \qquad (5)$$

$$\text{with} \qquad U_{t_{\pi/2}+\tau+t_\pi+t} = U_t \cdot U_\pi \cdot U_\tau \cdot U_{\pi/2} \qquad (6)$$

where σ_0 is the density operator in the initial state of the spins, $t_{\pi/2}$ and t_π are pulse length of the $\pi/2$ and π pulses. When the extrinsic magnetic field and the microwave field are parallel to z-axis and x-axis, respectively, the density operator is rewritten using the equations (4) as:

$$\sigma\left(t_{\pi/2}+\tau+t_\pi+t\right) = \cos(\Delta\omega\tau)\,S_z - \sin(\Delta\omega\tau)\cos(\Delta\omega t)\,S_x - \sin(\Delta\omega\tau)\cos(\Delta\omega t)\,S_y \qquad (7)$$

where $\Delta\omega$ is the difference between the microwave frequency and the resonate frequency shifted by local magnetic field i.e. the inhomogeneity of the magnetic field. The expectation of the density operator in y-axis is observable as ESE signal intensity:

$$\begin{aligned} I_y\left(t_{\pi/2}+\tau+t_\pi+t\right) &= Tr\left\{\sigma\left(t_{\pi/2}+\tau+t_\pi+t\right)\cdot S_y\right\} \\ &= \cos\left(\Delta\omega(\tau+t)\right) - \cos\left(\Delta\omega(\tau-t)\right) \end{aligned} \qquad (8)$$

The ESE signal intensity I_y reaches maximum when $t = \tau$.

Pulsed electron-electron double resonance (PELDOR) is one of the pulsed EPR methods which is applied to analyze the magnetic dipole interaction and the relative

position between spatially separated electron spins [18]. The magnetic dipole interaction is written as:

$$D = \frac{g_1 g_2 \beta^2}{hR^3}(1 - 3\cos^2\Theta) \quad (9)$$

where g_i is the *g*-factors for *i*-th electron spins, β is the strength of Bohr magneton and Θ is the angle between the distance vector ***R*** connecting the two spins and the vector of external magnetic field ***H***. In PELDOR measurement, another microwave frequency which excites the second electron spin is utilized between the $\pi/2$ and π pulses as shown in Figure G-6. The second microwave pulse inverts one of the spins, modulating the local magnetic field which the other spin feels. The ESE amplitude oscillates as following:

$$X(\tau') \propto 1 - p[1 - \cos(2\pi D\tau')] \quad (10)$$

where *p* is the spin fraction turned by the pumping pulse ($p < 1$). The strength of the dipole interaction, and hence the distance between two spins can be estimated from the oscillation pattern of the PELDOR spectra.

The recently determined high-resolution crystal structure of PS II provides new insights into the magnetic structure inferred by EPR measurements. Here, we applied PELDOR to analyze the spins in the OEC of PS II and clarify a detailed magnetic structure of the Mn cluster.

Figures

Figure G-1

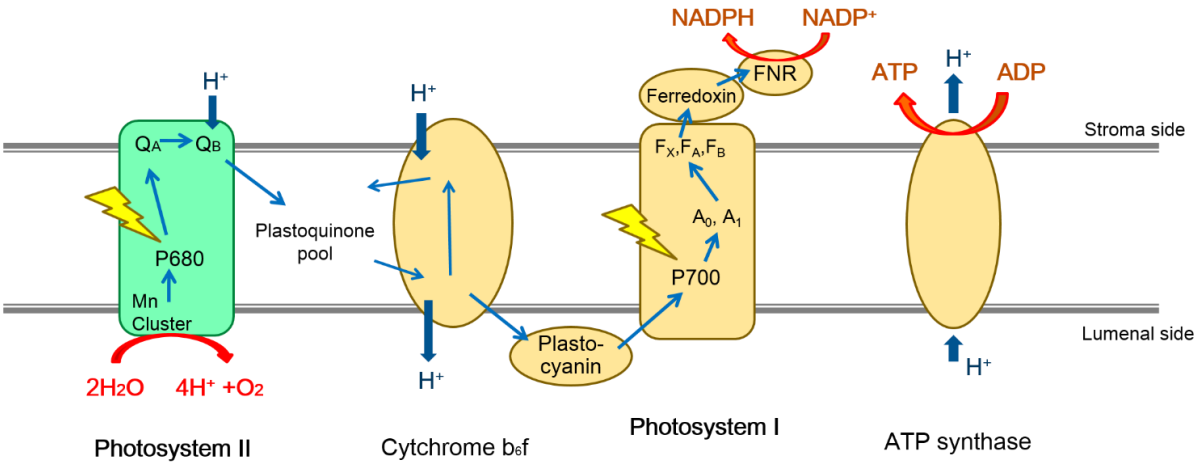

Figure G-1. Photosynthetic electron transport system in thylakoid membrane of higher plants.

Figure G-2

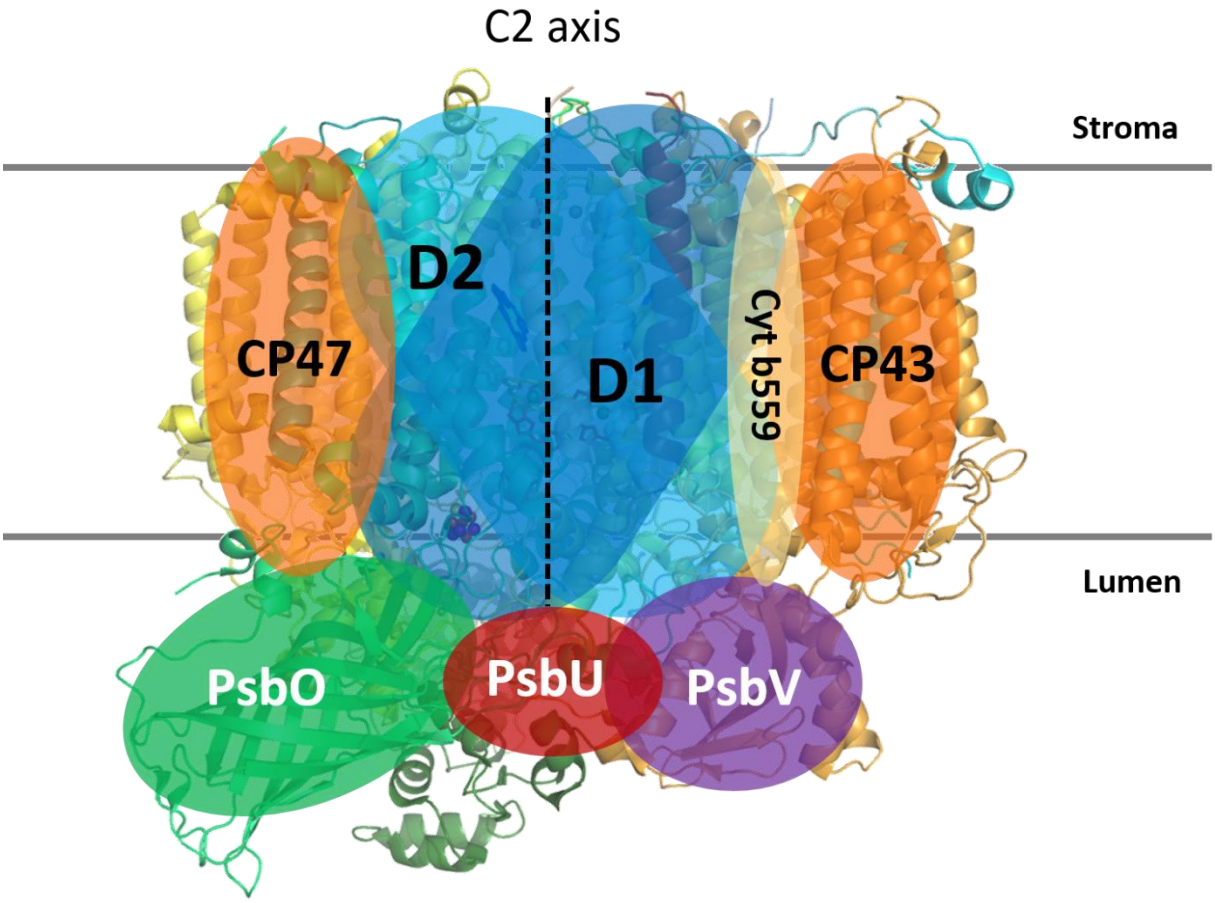

Figure G-2. Structure of PS II complex of *T. vulcanus*. D1 and D2 reaction center proteins are shown in *blue* and *light blue*, respectively, and antenna proteins CP43 and CP47 are shown in *orange*, and Cyt b559 is shown in *yellow*. The extrinsic subunits PsbO, PsbU, PsbV on the lumenal side of PS II are shown in *green*, *red* and *purple*, respectively.

Figure G-3

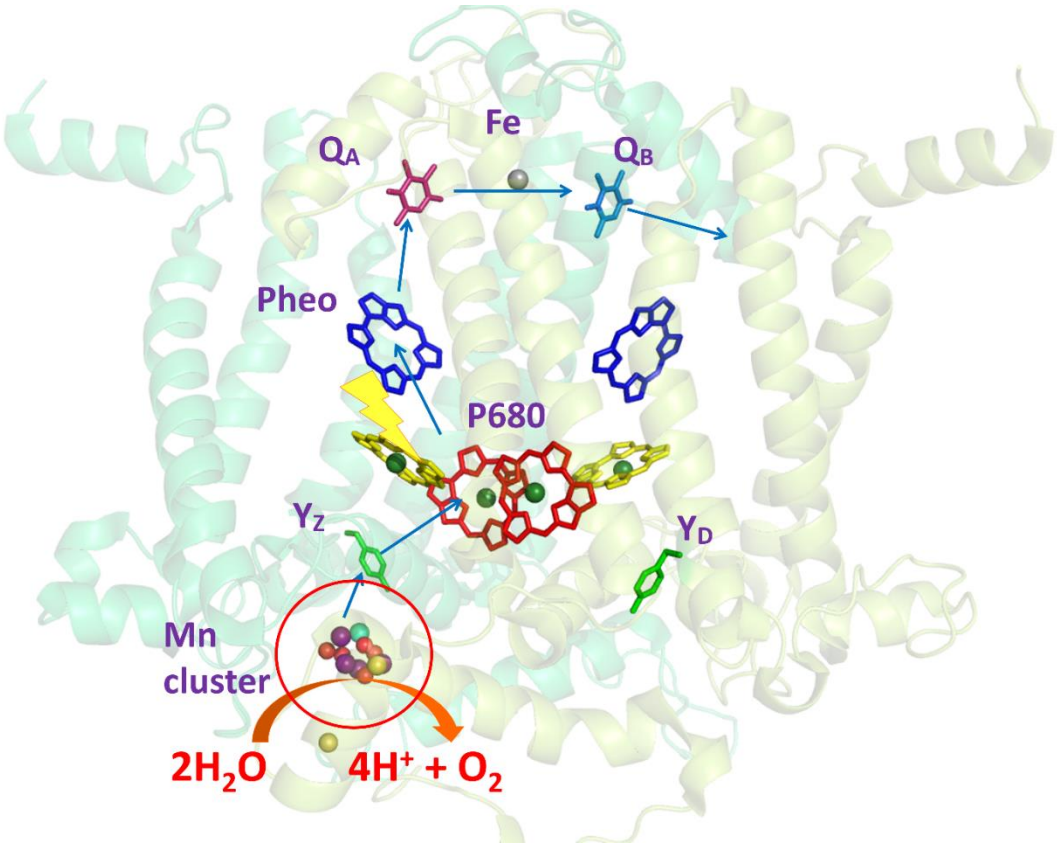

Figure G-3. Light-induced electron transfer chain in PS II core complex.

Figure G-4

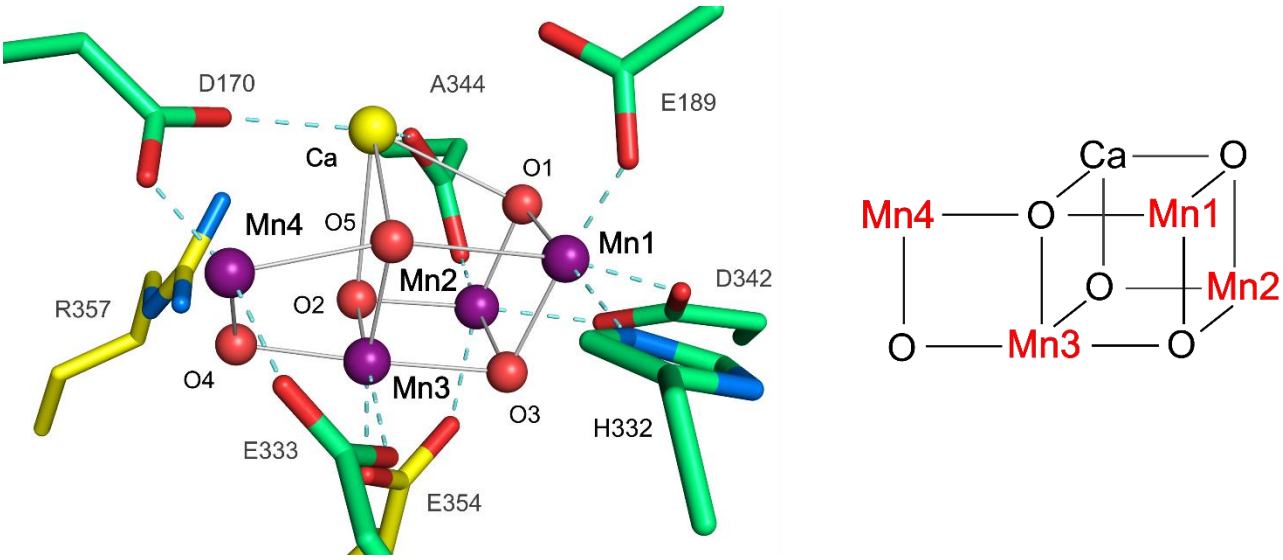

Figure G-4. (Left) The molecular structure of the oxygen-evolving complex revealed by X-ray crystallography (PDB: 4UB6). (Right) Covalent bonds representing the arrangement of the 4 Mn atoms, 1 Ca atom and 5 O atoms in OEC.

Figure G-5

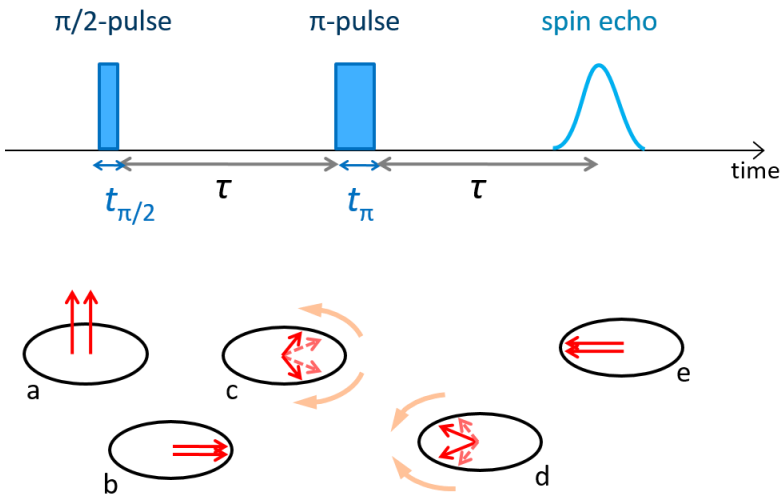

Figure G-5. Standard ESE pulse sequence and magnetization model. (a) At first the spins are magnetized to the external magnetic field. (b) The spin fraction is rotated by 90° by microwave pulse, then (c) allowed to diffuses due to the inhomogeneity of local magnetic field. (d) The spins are again rotated by 180° by microwave pulse, and (e) gathered to one direction which is observable as the spin echo signal.

Figure G-6

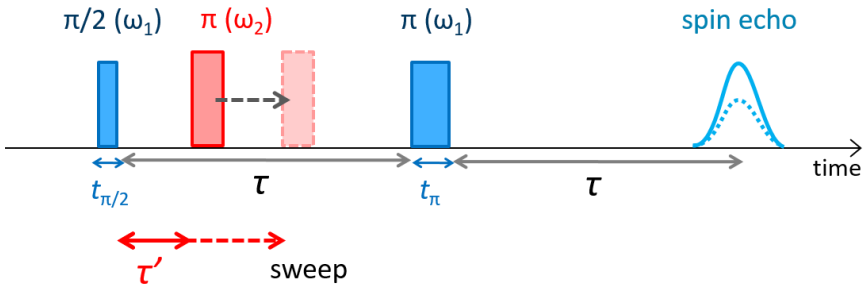

Figure G-6. Pulse sequence for the three-pulsed ELDOR measurement. The second microwave with the other frequency is applied between the two pulses for the ESE measurement.

Chapter I

Electronic structure of S_2 state Mn cluster of PS II

Chapter Introduction

The water oxidation reaction of photosynthesis is carried out by OEC. In this reaction, two water molecules are oxidized and an oxygen molecule is released through a cycle of five redox states of OEC, which is denoted as S_n (n = 0-4, shown in Figure I-1) [1-3]. The model of the catalytic cycle is investigated by Kok and coworkers, and the feature of the mechanism has been developed by spectroscopic studies. Each S_n state advances to S_{n+1} by a single light-driven reaction in PS II. Upon successive photoreactions, the OEC advances from the most stable state S_1 to the highest oxidation state S_4. This state is immediately converted to the lowest oxidation state S_0 associated with the generation of an oxygen molecule.

EPR spectroscopy has been performed to reveal the magnetic state of the intermediates of the Mn cluster. In the S_2 state, the Mn_4CaO_5 cluster represents an EPR multiline signal, which is a signpost for OEC in EPR studies. The multiline signal in the S_2 state is centered at g = 2 with a width of approximately 160 mT, and is characterized by 19-21 hyperfine lines with a spacing of 8.5-9 mT between each pair of adjacent lines [19]. This signal has been identified to an overall $\boldsymbol{S_T}$ = 1/2 ground spin state, which is proposed to arise from magnetically coupled Mn ions with a multinuclear complex of a Mn(III)-Mn(IV) pair in the S_2 state (reviewed in references [1-3, 20]). ^{55}Mn-pulsed ENDOR have described that the S_2 state Mn cluster is a multinuclear complex [21, 22]. Another EPR multiline signal was found in the S_0 state in the presence of methanol, which is composed of at least 26 peaks corresponding to an $\boldsymbol{S_T}$ = 1/2 ground state.

The oxidation states of the Mn atoms in each S state have remained to be clarified. The total oxidation state in each state proceeds one by one, so that a magnetic structure of S state can be estimated from spectroscopic differences relative to other S states. Kulik et al. suggested an oxidation state of (III, IV, IV, IV) for the four Mn ions in the S_2 state based on ^{55}Mn-pulsed ENDOR applied for as compared to that of the S_0 state [23]. The ^{55}Mn-pulsed ENDOR allowed to estimate four sets of hyperfine constants (hfc) for the four Mn ions, where the largest set of the hfc was assigned to the Mn(III) ion. Though the six exchange interactions *J* among the 4 Mn ions have not been experimentally obtained, several models have been proposed by calculation of hfc and spin projections of the Mn ions. Peloquin et al. proposed a model that the Mn ions are coupled antiferromagnetically [24] (described in Figure I-2, 1). Kulik et al. suggested a model in which one Mn(III) and two Mn(IV) ions are coupled antiferromagnetically [25], and one isolated Mn(IV) ion couples weakly to the three triangular Mn ions antiferromagnetically in a Y-shape structure (Figure I-2, 2). Siegbahn suggested a model connected with six exchange couplings based on calculation using EXAFS and medium resolution X-ray structures [26-28] (Siegbahn model, Figure I-2, 3 and 4). Cox et al. applied DFT calculation based on Q-band ^{55}Mn-pulsed ENDOR, supporting Siegbahn's model [29]. ESEEM studies indicated that the spin projection of the Mn ion ligating to ^{14}N is Mn(III) [30, 31]. His332 has been proposed to be a good candidate of a ligand to Mn(III) based on His332Glu mutagenesis studies and the X-ray structure.

PELDOR has been previously utilized to measure the distance between $Y_D^{\bullet}$ and the Mn

cluster in the S_2 state [32]. The distance between $Y_D^{\bullet}$ and the Mn cluster was evaluated to be 27 Å from the point-dipole approximation. However, the result is inconsistent with the recently obtained 1.9 Å PS II structure in which the distance between each Mn ion and the center of the aromatic ring of $Y_D^{\bullet}$ are approximately 30 ± 2 Å [16, 17]. The inconsistency may be attributed to delocalization of the electron spins among the 4 Mn atoms because it may include both of positive and negative signs of the electron spins. In this study, I performed the PELDOR measurement again and estimated the spin projections of each Mn ion in the S_2 state by calculating the PELDOR spectra.

Materials and Methods

Sample preparation

O_2 active PS II core complexes were isolated from a thermophilic cyanobacterium *Thermosynechococcus vulcanus* as described previously [33, 34] (provided by J-R. Shen, Okayama University). The samples were suspended in a buffer with 20 mM Mes (pH 6.0), 20 mM NaCl and 3 mM $CaCl_2$, and then transferred into EPR tubes.

Spinach PS II membranes were isolated as described previously [35, 36]. The PS II membranes were suspended in a buffer containing 400 mM sucrose, 20 mM NaCl and 20 mM Mes/NaOH (pH 6.5), and moved into EPR tubes.

For EPR measurement of the S_1 state, the PS II samples were pre-illuminated to oxidize $Y_D^{\bullet}$ and then they were dark-adapted for 2-3 h. The S_2 state of the samples was formed by photo-oxidation with white light illumination for 5 min at 200 K.

For the preparation of the membrane-oriented PS II sample, the apo-PS II membranes were suspended with the standard buffer containing 20 μM $MnCl_2$ at 1 mg of Chl/ml. Then the sample was centrifuged and the pellet was dried on an OHP sheet under a nitrogen gas flow for 15 h at 4 °C. The sheets were cut into 2.5 × 25 mm pieces and 6 pieces of them were placed in an EPR tube, and then it was frozen rapidly in liquid nitrogen (within 1 s). Glycerol was contained in the bottom of the EPR tube in order to improve the heat conductivity in the EPR tubes.

EPR measurement

CW EPR measurements were carried out with a Bruker ESP-300E ESR spectrometer with a gas flow temperature control system (CF935, Oxford Instruments, Oxford, GB).

Pulsed EPR spectra were recorded on a Bruker pulsed EPR spectrometer ESP-380E with an Oxford Instruments liquid helium cryostat. The ESE field swept spectra were measured using $\pi/2$-τ-π pulse sequence with a time interval τ of 200 ns between the microwave pulses. For the PELDOR measurements, a three-pulse PELDOR sequence was employed using $\pi/2$-τ-π sequence with the time interval τ of 1000 ns (described in Figure G-6). The pulse length of 16 ns for the $\pi/2$ pulse and 24 ns for the π pulses were utilized for both of the ESE and the PELDOR measurements. The ESP380 source was used for observation, and an microwave synthesizer (HP83751A, Hewlett-Packard) was used as the microwave source of 24 ns pumping pulse between the observation pulses [32, 37, 38].

PELDOR simulation

PELDOR signal amplitude $X(\tau')$ is a function of the time interval τ' between the 1st and 2nd microwave pulses [32, 37, 38] as described in the expression (9) and (10). The whole signal amplitude of the samples $I(\tau')$ is given by the integration of over whole angles:

$$I(\tau') = \iint X(\tau') \sin\theta \, d\theta d\varphi \qquad (11)$$

To calculate the PELDOR oscillation preciously, the spin density distribution on $Y_D^{\bullet}$ must be included. The dipole interaction D is rewritten as:

$$D = \sum_{ij} \rho_{ij} \frac{g_1 g_2 \beta^2}{h {R_{ij}}^3} \left(1 - 3\cos^2 \Theta_{ij}\right) \qquad (12)$$

where ρ_i is the spin density at the i-th (i = 1-7) carbon/oxygen atom of the $Y_D^{\bullet}$ molecule and ρ_j is the spin projection at the j-th (j = 1-4) Mn atom in OEC. R_{ij} is the distance between the i-th carbon/oxygen atom of the $Y_D^{\bullet}$ and the j-th Mn atom. Θ_{ij} is the angle between the external magnetic field $\boldsymbol{H}$ and the distance vector $\boldsymbol{R_{ij}}$.

The PELDOR intensities for oriented PS II membranes are given by:

$$I(\tau') = \iint X(\tau')G(\theta - \theta_0)\sin\theta\, d\theta d\varphi \quad (13)$$

with

$$G(\theta - \theta_0) = \exp\left[-\frac{1}{2}\left(\frac{\theta-\theta_0}{\Delta}\right)^2\right] \quad (14)$$

where θ_0 is the angle between the membrane normal $\boldsymbol{n}$ and external magnetic field $\boldsymbol{H_0}$ (see Figure I-3). Δ is the distribution angle of the mosaic spread of the oriented membranes, and $G(\theta\text{-}\theta_0)$ is the mosaic spread function which is assumed to follow Gaussian distribution. The z-axis of the PS II core complex was set to the membrane normal $\boldsymbol{n}$ along with the pseudo C_2 symmetric axis of PS II. The coordinates of the atoms on $Y_D^{\bullet}$ and the OEC were obtained from the 1.9 Å resolution X-ray structure (PDB: 3ARC). The spin density distribution on $Y_D^{\bullet}$ are shown in Figure I-4, which was obtained from the previous studies [39-42].

Spin projection

Spin Hamiltonian of the Mn cluster is given by follows:

$$\mathcal{H} = \sum_i [\boldsymbol{H_0}\cdot\boldsymbol{g_i}\cdot\boldsymbol{S_i} + \boldsymbol{I_i}\cdot\boldsymbol{a_i}\cdot\boldsymbol{S_i} + \boldsymbol{S_i}\cdot\boldsymbol{D_i}\cdot\boldsymbol{S_i}] - \sum_{i<j} J_{ij}\cdot\boldsymbol{S_i}\cdot\boldsymbol{S_j} \quad (15)$$

where $\boldsymbol{g_i}$ is the *g*-tensor, and $\boldsymbol{S_i}$ and $\boldsymbol{I_i}$ are the operators of the electron spin and nuclear spin of the *i*-th Mn ion, respectively. $\boldsymbol{D_i}$ is the zero-field splitting (ZFS) tensor for the *i*-th Mn ion, and $\boldsymbol{a_i}$ is the hyperfine tensor of the *i*-th ion. J_{ij} is the exchange interaction between the *i*-th and *j*-th ion. When the ZFS effects are neglected, the spin Hamiltonian can be rewritten as:

$$\boldsymbol{\mathcal{H}} = \mu_B \boldsymbol{H_0}\cdot\boldsymbol{g_i}\cdot\boldsymbol{S_T} + \sum_i \boldsymbol{I_i}\cdot\boldsymbol{A_i}\cdot\boldsymbol{S_T} - \sum_{i<j} J_{ij}\cdot\boldsymbol{S_i}\cdot\boldsymbol{S_j} \quad (16)$$

where $\boldsymbol{A_i}$ is the effective hyperfine tensor of the *i*-th ion, and $\boldsymbol{S_T}$ is the total spin state with

$\boldsymbol{S_T}$ = 1/2 for the S_2 state Mn cluster. The effective hyperfine tensor $\boldsymbol{A_i}$ and the local hyperfine tensor $\boldsymbol{a_i}$ are related by the following equation:

$$\boldsymbol{A_i} = \rho_i \boldsymbol{a_i} \tag{17}$$

where ρ_i is the spin density of the *i*-th ion. When the ZFS effects are neglected, the anisotropic portions of ρ_i can be neglected. The relationship between the isotropic portions of $\boldsymbol{A_i}$, $\boldsymbol{a_i}$ and ρ_i is given by:

$$\boldsymbol{A_{i,iso}} = \rho_{i,iso} \boldsymbol{a_{i,iso}} \tag{18}$$

where $\rho_{i,iso}$ is identified as the spin projection and is defined by the value of the electron spin $\boldsymbol{S_i}$ as:

$$\rho_{i,iso} = \frac{\langle S_i S_T \rangle}{S_T(S_T+1)} \tag{19}$$

The values of the spin operator S_i for each Mn atom in the S_2 state have not been evaluated experimentally. The effective hyperfine constants $A_{i,iso}$ have been obtained by X- and Q-band ENDOR measurements in the S_2 state, and the intrinsic hyperfine constants a_{iso} were estimated to be -165 to -225 MHz for Mn(III) and -187 to -253 MHz for Mn(IV), respectively [24, 29]. The possible range of the spin projections are shown in Table 1.

Results

PELDOR experiments for the non-oriented PS II samples

Figure I-5 shows the ESE field swept spectra of *T. vulcanus* PS II core complex in (A) the S_2 and (B) the S_1 states. The S_2 multiline signal with 60 mT width centered at $g = 2$ is represented, which arises from the $S = 1/2$ ground spin state of the Mn cluster. In the S_1 state, no such signal except for the signal arising the narrow signal centered at $g = 2$ arising from $Y_D^{\bullet}$ was observed.

A three-pulse PELDOR sequence was utilized for the measurement, where the 1st and 3rd pulses were applied to the S_2 multiline signal for observation (filled array) and the 2nd pulse for pumping pulse was applied to $Y_D^{\bullet}$ (blank array). Figure I-6 represents (A, B) PELDOR signals between $Y_D^{\bullet}$ and the S_2 state Mn cluster in the (A) *T. vulcanus* and (B) spinach PS II samples, whose oscillations correspond to the magnetic dipole interaction between $Y_D^{\bullet}$ and the S_2 state Mn cluster. The PELDOR oscillation in the spinach PS II corresponded to the previously reported spectrum [32]. The PELDOR oscillation in *T. vulcanus* PS II was very similar to that observed in the spinach sample, which indicates that the PS II isolated from *T. vulcanus* and spinach is similar in terms of the structure of the lumenal side of the core complex. Slight distortion in trace A might be ascribed to overlapping of the Chl^+ signals on $Y_D^{\bullet}$, which was about 15 % of the signal intensity for *T. vulcunus*. Chl^+ is formed by long illumination (Figure I-7). The PS II sample isolated from *T. vulcanus* is core complex, which has much less antenna proteins than the PS II membranes from spinach, therefore the light might be relatively strong for *T. vulcanus* PS II.

The experimental signals correspond to the calculation with the point-dipole approximation for the distance of 27 Å (Figure I-6C). However, in the high-resolution X-ray structure, the distances between the center of $Y_D^{\bullet}$ aromatic ring and the Mn ions are 29.1, 31.9, 31.1 and 30.1 Å for the Mn1-4 ions, respectively. These distances are close to 30 Å, however, the oscillation pattern calculated with 30 Å point dipole approximation shown in trace D is apparently different from the experiments. This inconsistency corresponds to the different contributions of the spin projections among the four Mn ions in OEC. Thus, it is needed to calculate the accurate PELDOR pattern using the spin density distribution on $Y_D^{\bullet}$ and the Mn cluster including their coordinates.

PELDOR simulations calculated with spin projections

Table 1 shows the parameters of the spin projections on the Mn atoms of the S_2 multiline signal which have been calculated based on the EPR simulation, ENDOR, and DFT calculations [24, 29, 43]. Peloquin et al. have reported the spin projections of 1.7, 1.27, -1 and -0.99 for the four Mn ions based on simulation of their ENDOR spectra [24]. There has been no one-to-one assignment of the spin projections to the four Mn ions, so that we calculated several combinations of the projections on the four Mn atoms with assumption of structural models. Assuming that two of the spin projections of -1 and -0.99 are approximated to -1, twelve kinds of the combinations of the Mn atoms and the projections are possible. The maximum spin projection of 1.7 was assumed to be on Mn(III), which were assigned to (a1-a3) Mn1, (b1-3) Mn2, (c1-3) Mn3 and (d1-3) Mn4. The other spin projection with a positive sign of 1.27 was assigned to (a1-3) Mn2-4, (b1-3) Mn1, 3, 4, (c1-3) Mn1, 2, 4, and (d1-3) Mn1-3, respectively. The numbering of the Mn ions is based on the X-ray structure reported by Umena et al. [16]. The

patterns of the combinations of spins on the Mn cluster are shown in Figure I-8. Figure I-9 represents the simulated PELDOR spectra based on the possible combinations of the Mn ions and spin projections. The simulated signals were calculated using equations 3 and 4, as well as the spin projections previously calculated by Peloquin et al. [24]. The broken lines are corresponding to the positive peaks of the experimentally obtained PELDOR oscillation. The oscillation patterns for the spin projection combinations b2, c2 and d2 were clearly mismatched to the experiment. The simulated oscillation patterns for the spin projection combinations a1-3 and d1 were similar to the experimental data, where Mn1 has the largest spin projection of 1.7, and Mn4 has the largest projection and Mn1 has the other positive projection of 1.27. The patterns where Mn1 has the larger positive projection (a1-3) relatively seem to match. However, these calculated patterns (a1-3 and d1) did not clearly equal to the experimental oscillation. Additionally, none of the parameters shown in other literatures matched to the experiment as well [23, 29, 43].

In the previous reports, other values of the spin projections were also evaluated to be in the range [29]. Because the A_{iso} of 165-225 MHz for single Mn(III) ion and 187-253 MHz for single Mn(IV) ion are possible in various compounds, the range of the spin projections were estimated to be [1.39 ~1.89, 0.99 ~1.34, -1.11 ~ -0.82, -1.02 ~ -0.75] for the four Mn ions. We applied these spin projections to calculate the PELDOR oscillations which fit to the experimental results. For the calculation, the spin projections were varied by 0.01 in the range of [1.2 ~ 2.0, 0.9 ~ 1.5, -1.2 ~ -0.65, -1.2 ~ -0.65], increasing the margin by 10%. The twelve kinds of combinations of the positive and the negative spin projections whose sum was assumed to be 1.00 were tried. We

chose the combinations of the spin projections and the positions of Mn atoms, which fit to the experimental oscillation with a negative peak at τ' = 200 ns and positive peaks at τ' = 440 and 800 ns, allowing the maximum error limit of 5% for the peak positions.

Figure I-10 shows the three fitting combinations, which is corresponding to a2, a3 and d1 shown in Figure I-9. The fitting ranges of the spin projection for each combinations were represented in Table 2. The largest positive spin projection was denoted as [++], the smaller positive one was denoted as [+], and the negative spin projections were denoted as [-]. The order of the signs represents the position of the Mn ions corresponding to Mn1-4. First, the largest positive spin projection is located at Mn1 position and the other smaller positive one is located at Mn3, denoted [++, -, +, -] (Figure I-10, trace B). Second, the largest positive spin projection is located at Mn1 and the smaller positive one is located at Mn4, denoted [++, -, -, +] (trace C). Finally, the largest positive projection spin is located at Mn4 and the smaller positive one is located at Mn1, denoted [+, -, -, ++] (trace D). In these three combinations, Mn1 has the positive projection and Mn2 has the negative projection, and Mn3 and Mn4 have the opposite sign to each other. It is required that the Mn ions are connected antiferromagnetically between Mn1 and Mn2, and between Mn3 and Mn4.

PELDOR experiment with the oriented PS II samples

The combinations [++, -, +, -], [++, -, -, +] and [+, -, -, ++] gave the same PELDOR oscillations for the non-oriented PS II complex. To distinguish these combinations, I measured the angular dependence of the PELDOR oscillation using the oriented PS II membranes. The mosaic spread angle for the oriented sample was evaluated by the

g_Z peak of the Cyt b559 signal measured with CW EPR spectroscopy shown in Figure I-11. The signal intensities for the g_Z peak in the oriented PSII membranes depends on the angle θ between the membrane normal ***n*** and the extrinsic magnetic field $\boldsymbol{H_0}$, which reach the maximum when $\boldsymbol{H_0}$ is perpendicular to ***n*** (θ = 90º), and the minimum when $\boldsymbol{H_0}$ is parallel to ***n*** (θ = 0º). The mean square deviation Δ was evaluated to be 17 ± 0.5° by fitting with the Gaussian function defined in equation 14.

Figure I-12 shows the PELDOR signals at (a) θ = 0° and (b) θ = 90° in the oriented sample. At the angle of θ = 0º, the PELDOR signal appears to include only one frequency because the angle between dipole vector ***R*** between $Y_D^{\bullet}$ and the Mn cluster and $\boldsymbol{H_0}$ is uniquely determined within the distribution angles. The negative peaks with τ' = 220 ns and τ' = 620 ns at θ = 0° shifted to τ' = 180 ns and τ' = 580 ns at θ = 90°, respectively. The positive peaks with τ' = 430 ns and 810 ns at θ = 0° stayed the same position at θ = 90º. An inflection with τ' = 300 ns appeared at θ = 90º. The PELDOR oscillations for the oriented membranes were calculated reflecting the equation 13. The PELDOR signals were fitted at the negative and positive peaks at τ' = 220, 430 and 810 ns with θ = 0º and at τ' = 180, 430 and 810 ns with θ = 90º with the maximum error limit of 5% for each peak. The best fitting combinations of the Mn atoms and the spin projections were provided in the model where Mn1 has the larger positive projection, Mn3 has the smaller positive projection and Mn2 and Mn4 have negative projections, denoted [++, -, +, -]. The possible range of the largest positive spin projection, which was assumed to belong to Mn(III) in the literature, were 1.87–2.0 for the model [++, -, +, -]. The fitting range of the spin projections are represented in Table 2. The red lines in Figure I-12 shows the signals best matching within the allowed ranges (i.e., 1.97, -1.2,

1.19 and -0.96 for Mn1-4, respectively). The other combinations of the Mn atoms and the spin projections showed the similar PELDOR oscillations but different from the fitting oscillation.

The models could be distinguished especially in terms of the first negative peak positions. Figure I-13 represents the relation between the values of the spin projections and the initial negative peaks in the calculated spectra for θ = 90º. The gray parts represent the peak positions fitted to the experimental signal within 5%. Panel A shows the largest spin projection. Circles show the spin projection of Mn1 in the model [++, - , +, -] which were fitting in the range of 1.87-2.00. Crosses and squares show the spin projections of Mn1 in the model [++, - , - , +] and Mn4 in the model [+, - , - , ++], respectively. The [++, -, -, +] and [+, -, -, ++] models did not match within the 5 % variation. The best fitting spin projections were 1.38-1.41 for [++, -, -, +] and 1.21-1.5 for [+, -, -, ++] models, which are relatively lower than that in the model [++, -, +, -]. Panel B represents the smaller positive spin projections. Panel C show the negative spin projections for Mn2 in the all models, and panel D shows the other negative projections for Mn4 in the model [++, -, +, -] or Mn3 in the model [++, -, -, +] and [+, -, -, ++]. The possible ranges of the spin projections for these three models are listed in Table 2. The simulated signals for [++, -, -, +] and [+, -, -, ++] models are shown as the blue and green lines in Figure I-12, respectively, which were the closest to the allowed peak positions shown as gray area in Figure I-13.

Discussion

To date, the magnetic structure of the Mn cluster has been investigated by EPR spectroscopy, and several studies have proposed the structure and function of OEC. ^{55}Mn-pulsed ENDOR studies have evaluated the hyperfine couplings of four manganese ions in the S_0 and S_2 states, and led to the conclusion that the valences of the four Mn ions are (III, III, III, IV) in the S_0 state and (III, IV, IV, IV) in the S_2 state [23, 24]. However, the individual valence of each Mn ion and the couplings between the Mn ions have remained to be incompatible with the molecular structure yet.

It has been difficult to evaluate the clear relationship between the X-ray crystal structure and the magnetic interactions measured by EPR spectroscopy. The most favorable model for the structure is a '3+1' Mn tetramer proposed by the ^{55}Mn-pulsed ENDOR results. In this model, the four Mn ions form a Y-shape structure, where the triangle unit denoted as MnBCD is strictly coupled to each other, and the fourth Mn atom denoted as MnA is coupled to MnB, one of the Mn ions which form a triangle unit. The designated MnA, B, C and D corresponded to that of Mn4, Mn3, Mn2 and Mn1 in the 1.9 Å resolution crystal structure, respectively. However, it has not been clarified which Mn atom is Mn(III) in the Y-shape model. Kulik et al. suggested that MnA or MnC is Mn(III) [25]. MnA was regarded as Mn(III) by comparing the ENDOR results in the S_0 and S_2 states. On the other hand, Charlot et al. have attributed Mn(III) to MnC or MnD, which is in the trimer side [43]. In these models, MnB is located at the center of the Y-shaped structure and is not suggested to be Mn(III). Siegbahn et al. proposed the model in which Mn atoms are connected with six exchange couplings *J* based on quantum chemical calculations and EXAFS spectroscopy [29, 44, 45]. In this model, the

MnA-MnB and MnC-MnD couplings are assigned to be antiferromagnetic, where the MnC and MnD are not distinguished from each other from an electronic perspective. Siegbahn's model is consistent with the Kulik model if MnC is assigned to be Mn(III). The location of the Mn(III) was assigned to the largest hyperfine couplings of the four Mn ions in these models [24, 25].

To clarify the ambiguities of the magnetic interactions between the Mn atoms in the S_2 state Mn cluster, we measured the PELDOR spectra between $Y_D^{\bullet}$ and the S_2 multiline signals in the non-oriented and oriented PS II membranes, and assigned the spin projections of the Mn ions to the positions obtained from the X-ray structure. The result suggested that (1) the Mn ion denoted as Mn1 is Mn(III) and the other Mn ions Mn2-4 are Mn(IV); (2) the most likely spin projections of the Mn ions are obtained with the [++, -, +, -] model, where Mn1-4 have the spin projections of 1.97, -1.19, 1.17 and -0.95, respectively. The result is consistent with the ^{14}N ESEEM reports, where ^{14}N of His332 directly binds to Mn(III) ion, whose spin projection is estimated to be close to 2 from the ^{14}N parameters [30, 31]. The result (2) gives the signs of the exchange couplings *J* between the Mn ions as shown in Figure I-14. The couplings between Mn1-Mn2 and Mn3-Mn4 are assigned to be antiferromagnetic, which is consistent with the Siegbahn's model. According to the X-ray crystal structure, the distances between the Mn atoms are 2.8-2.9 Å for Mn1-Mn2 and Mn2-Mn3 pairs. These Mn pairs are the closest in the OEC. Thus it should be stable if the pairs of Mn1-Mn2 and Mn3-Mn4 couple antiferromagnetically. The calculation took into account the assumption that the wide range of 1.2-2.0 of the largest spin projection is corresponding to Mn(III); however, the largest spin projection was less than 1.5 both in the [++, -, -, +] and [+, -, -, ++]

models. This result is inconsistent with the ^{14}N ESEEM result. It is remarked that the PELDOR spectra and the calculation directly assigned the spin projections to the location of the Mn ions in the OEC including the coordinates. They are consistent with the already proposed models assuming that the MnC(Mn2) and MnD(Mn1) are arbitrary from an electronic perspective [25, 29, 45].

Ames et al. proposed that Mn1 and Mn4 have the same sign of the spin projection, which is corresponding to the [++, -, -, +] model for the S_2 state Mn cluster. Additionally their DFT simulation based on ^{55}Mn ENDOR indicated that Mn1 does not bind to O5 in the S_2 state and it extend the distance between Mn4 and O5 by approximately 0.3 Å than that in the S_1 state, which had been revealed by the X-ray crystallography [45]. We checked the influence on the PELDOR results by modifying the coordinates of Mn4 ion by 0.3 Å. Trial simulations represented that the peak positions of the PELDOR spectra are changed by less than 5 % for the [++, -, +, -] and [++, -, -, +] models, and less than 10% for the [+, -, -, ++] model. Despite of the structural modification, the best matched model was still [++, -, +, -] in these cases. These results indicate that the structural change of Mn4 by 0.3 Å is too small to affect the PELDOR results, and is not a critical reason for the inconsistency in these models. Another possible reason for the inconsistency might be the anisotropic effects of the projection factors because the present PELDOR calculation did not include the anisotropic factors. According to the DFT simulations, the anisotropic spin projections on the Mn ions are proposed to be large, which might alter the PELDOR spectra [29]. By using the DFT parameters, the anisotropic effect of spin projection would clarify the information of the S_2 state in detail.

In conclusion, we applied the PELDOR measurement to determine the electronic structure of the Mn_4CaO_5 cluster in the S_2 state. Calculation considering the spin projections of the Mn cluster and the spin density distribution on $Y_D^{\bullet}$ allowed us to make relationship between the location and the spin projections of the Mn atoms. The best fitting parameters of the spin projections were 1.97, -1.19, 1.17 and -0.95 for Mn1-4, respectively. The results indicated that Mn1 is the Mn(III), and the model where Mn1 and Mn3 have the positive sign and Mn2 and Mn4 have the negative sign of the spin projections in the S_2 state. The coupling of Mn1-Mn3 was assigned to be ferromagnetic, and the couplings Mn1-Mn2 and Mn3-Mn4 were assigned to be antiferromagnetic.

Figures

Figure I-1

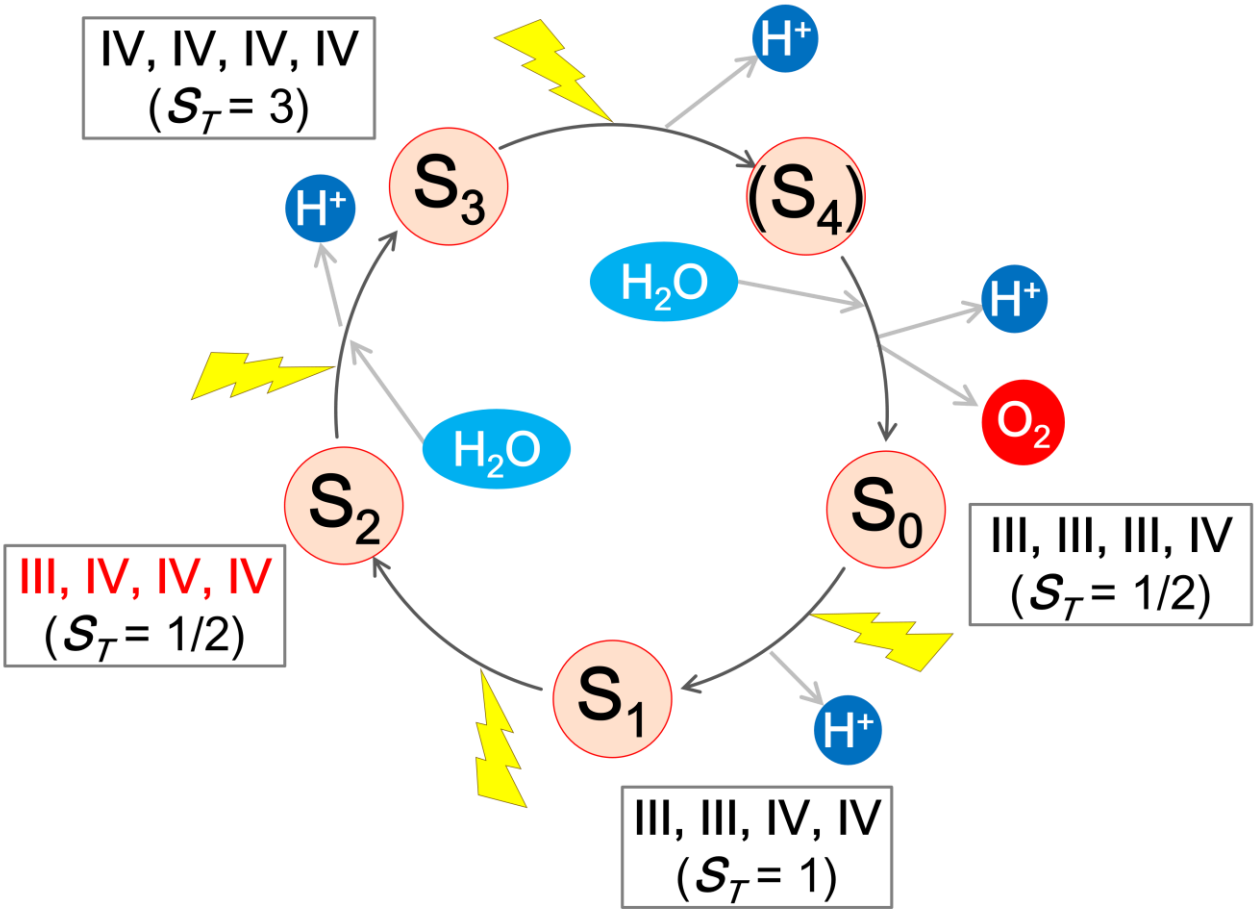

Figure I-1. The catalytic cycle and the oxidation states of the Mn cluster. The numbers in the boxes show the proposed combination of the valent Mn atoms and the total spin states in the respective intermediate states.

Figure I-2

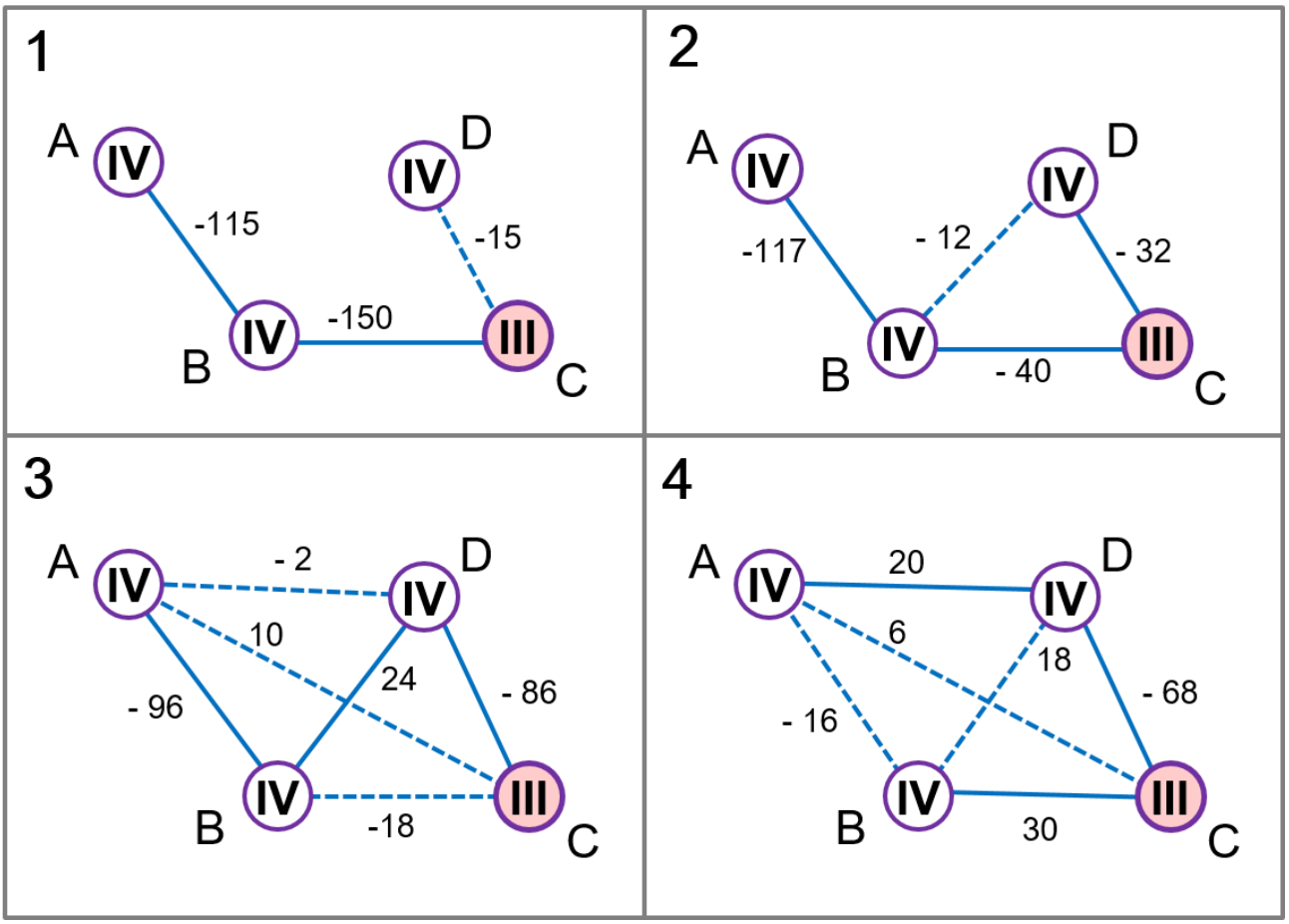

Figure I-2. Electro-magnetic models for the S_2 state Mn cluster proposed by (1) Peloquin et al. and (2) Kulik et al. with DFT calculations, (3, 4) Pantazis et al. with (3) EXAFS spectroscopy and with (4) DFT simulation based on Siegbahn model. The numbers represent the strength of the interaction in the unit of cm^{-1}.

Figure I-3

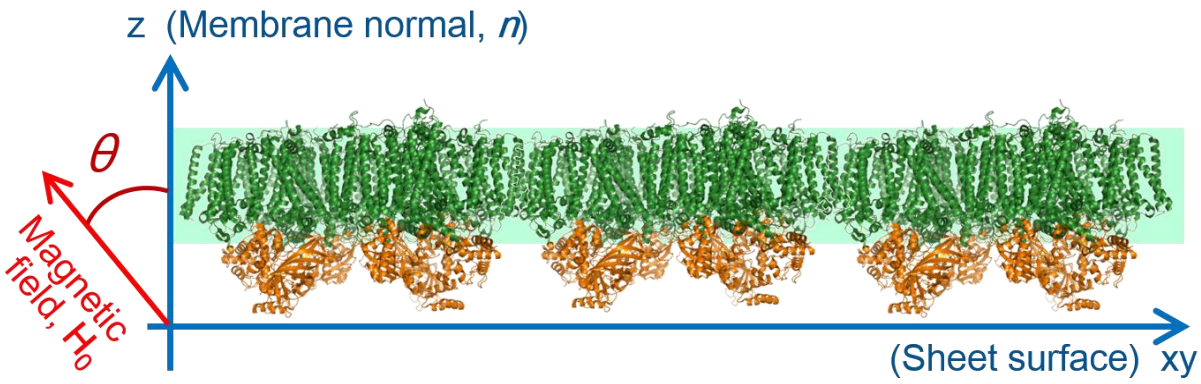

Figure I-3. Structural model of the oriented PS II membranes. Z-axis is corresponding to the membrane normal ***n***. θ was determined to be the angle between ***n*** and the extrinsic magnetic field $\boldsymbol{H_0}$.

Figure I-4

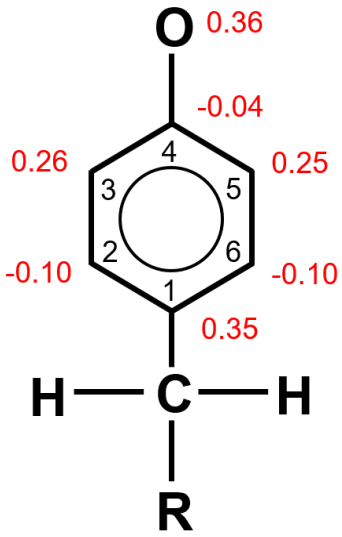

Figure I-4. The spin density distribution on tyrosine radical in protein.

Figure I-5

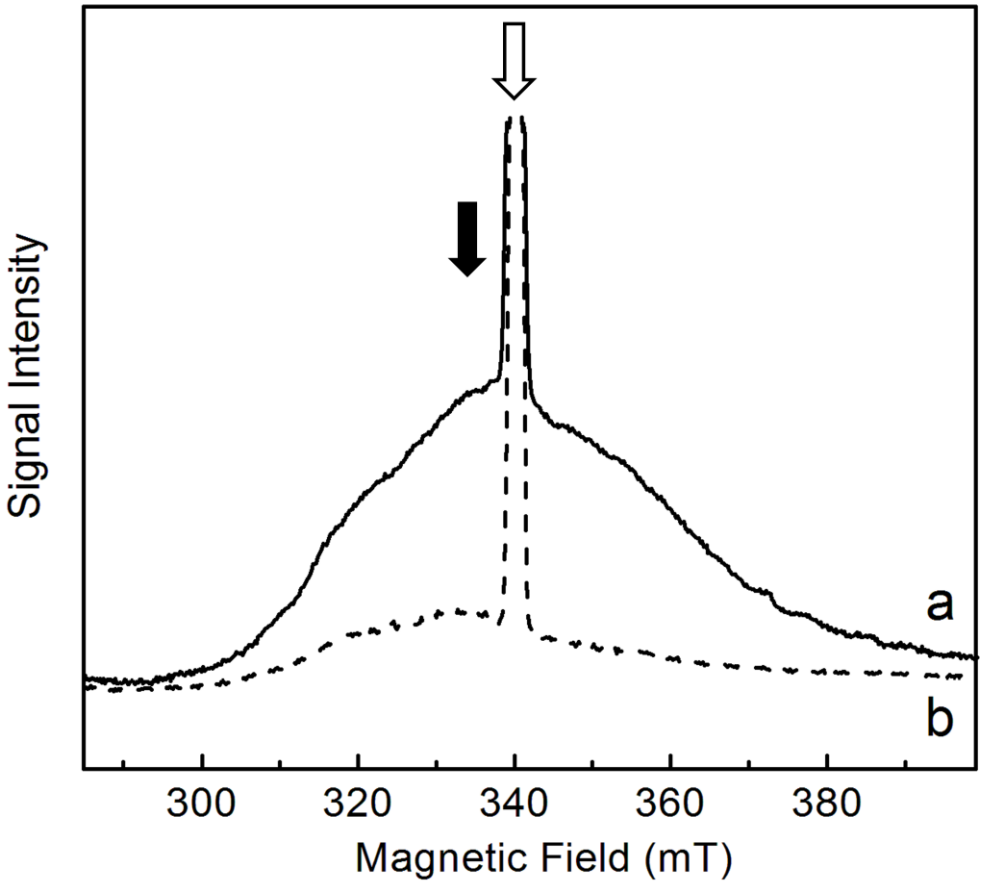

Figure I-5. ESE field swept spectra of *T. vulcanus* PS II core complex in (a) the S_2 state and (b) the S_1 state. The saturated signals arising from $Y_D^{\bullet}$ at 340 mT were cut off. The arrows represent the resonant magnetic field utilized for (filled) the observation pulses and (blank) the pumping pulses to measure the PELDOR spectra. Experimental conditions: microwave frequency, 9.60 GHz; interval time between the microwave pulses, 200 ns; repetition time, 2 ms; temperature, 4 K.

Figure I-6

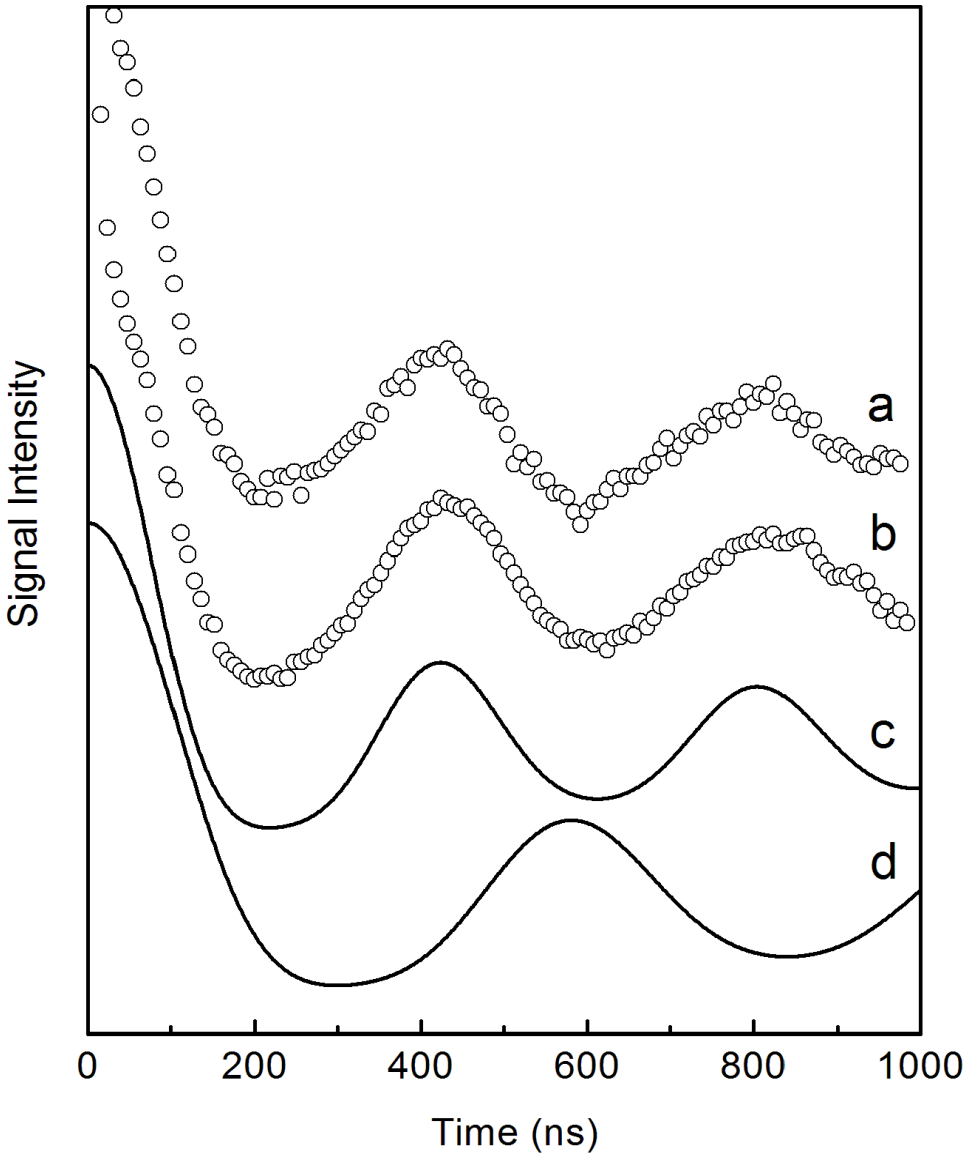

Figure I-6. (A, B) Experimental three-pulsed ELDOR signals of the interaction between $Y_D^{\bullet}$ radical and the Mn cluster in the S_2 state of PS II isolated from (A) *T. vulcanus* and (B) spinach. (C, D) Simulated PELDOR oscillations assuming a point-dipole interaction between spin $\boldsymbol{S}$ = 1/2 centers with the distance of (C) 27 Å and (D) 30 Å. The frequencies applied for the measurements were decided as shown in Figure I-5. Experimental conditions: observation microwave frequency, 9.61 GHz; pumping microwave frequency, 9.73 GHz; time interval between the first and the third pulses, 1000 ns; repetition time, 2 ms; magnetic field, 348 mT; temperature, 4 K.

Figure I-7

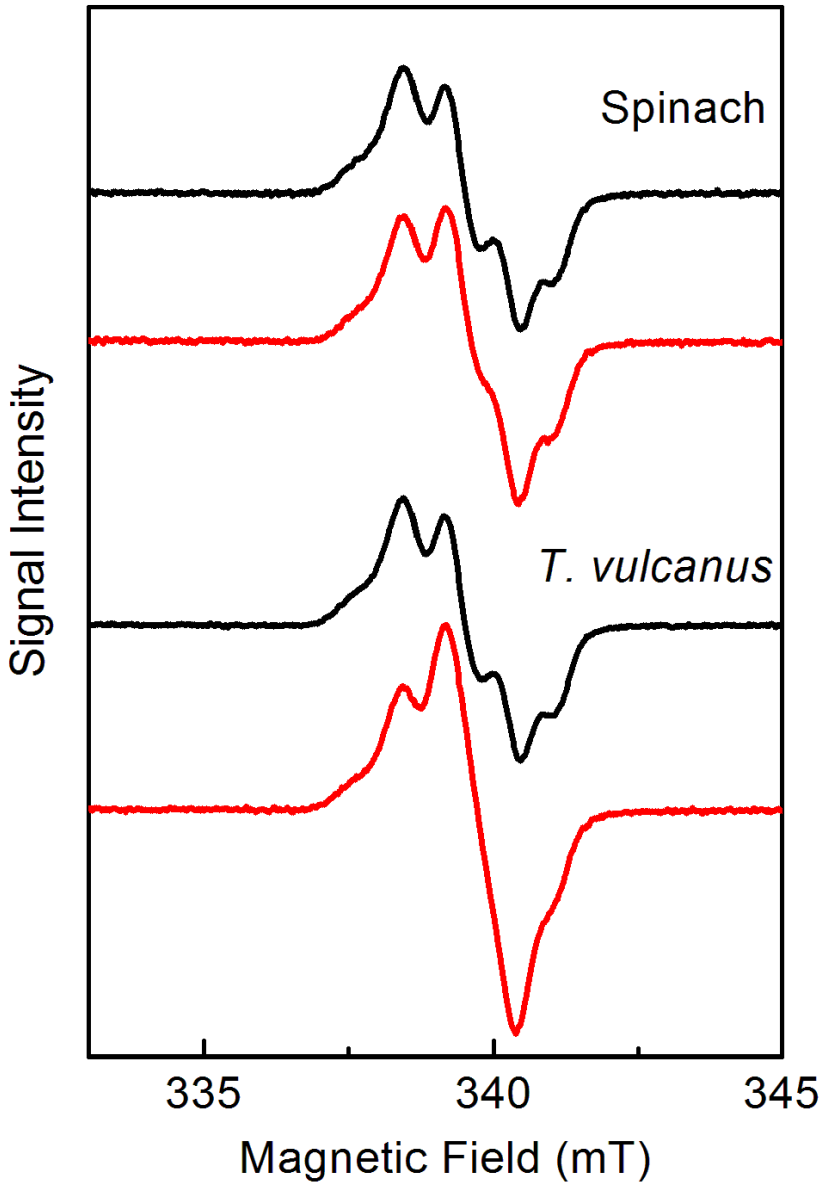
Spinach
T. vulcanus
Signal Intensity
335
340
345
Magnetic Field (mT)

Figure I-7. CW-ESR spectra arising from $g = 2$ of PS II in (black lines) the S_1 state and (red lines) the S_2 state isolated from spinach and *T. vulcanus*. Experimental conditions: microwave frequency, 9.59 GHz; microwave power, 50.5 μW; modulation amplitude, 0.4 mT; temperature, 170 K.

Figure I-8

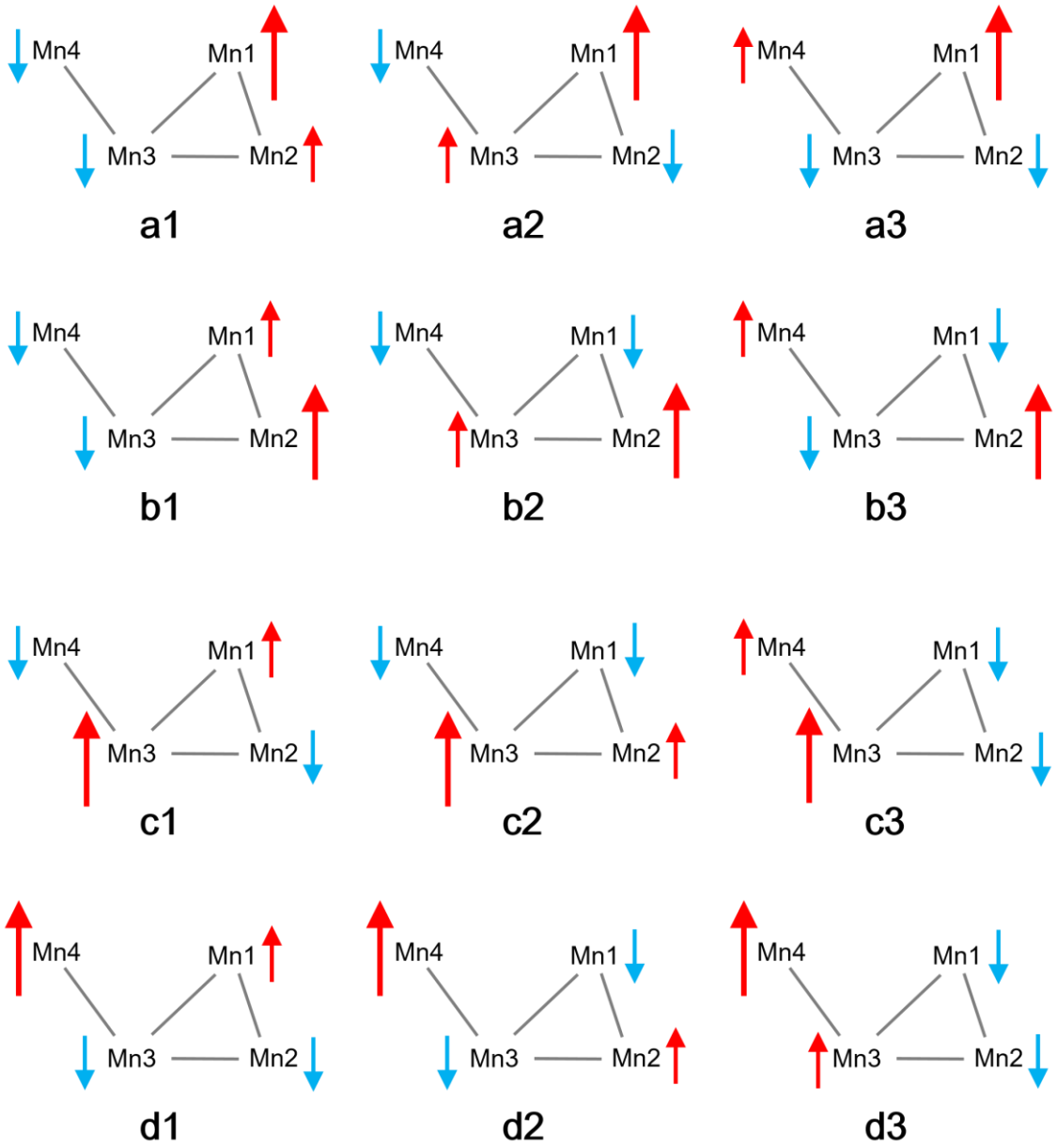

Figure I-8. Spin projection patterns considered for PELDOR calculation using the parameters of 1.7, 1.27, -1 and -1. Pairs of the Mn atoms which have relatively close distance were connected. The positive spin projections are shown in red and the negative spin projections are shown in blue. The larger positive spin projection was suggested to be Mn(III), which is at Mn1 for (a1-3), Mn2 for (b1-3), Mn3 for (c1-3) and Mn4 for (d1-3), respectively. The other positive spin production 1.27 was assumed to be on Mn2-4 for the model (a1–3), Mn1, 3, 4 for (b1–3), Mn1, 2, 4 for (c1–3), and Mn1-3 for (d1–3), respectively.

Figure I-9

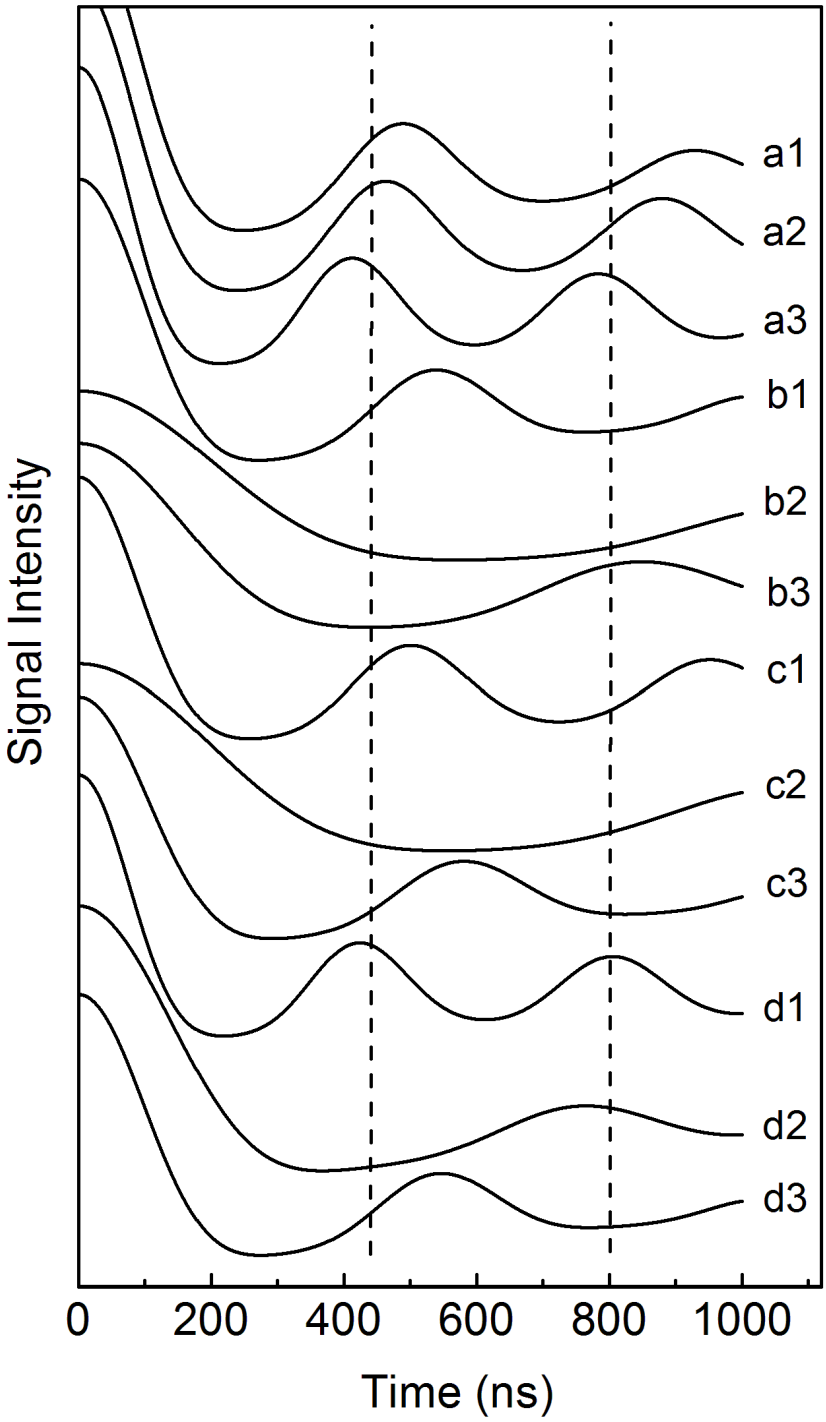
Signal Intensity
a1
a2
a3
b1
b2
b3
c1
c2
c3
d1
d2
d3
0
200
400
600
800
1000
Time (ns)

Figure I-9. Calculated PELDOR signals of the interaction between the $Y_D^{\bullet}$ and the S_2 state Mn cluster considering the spin density distribution on $Y_D^{\bullet}$ and the spin projections of Mn atoms. The spin projection parameters of 1.7, 1.27, -1 and -1 evaluated in the literature were used for the calculation. The combinations of the spin projections was assumed to the models as illustrated in Figure I-8. The dotted lines correspond to the experimentally obtained positive peaks (τ' = 440, 800 ns) represented in Figure I-6.

Figure I-10

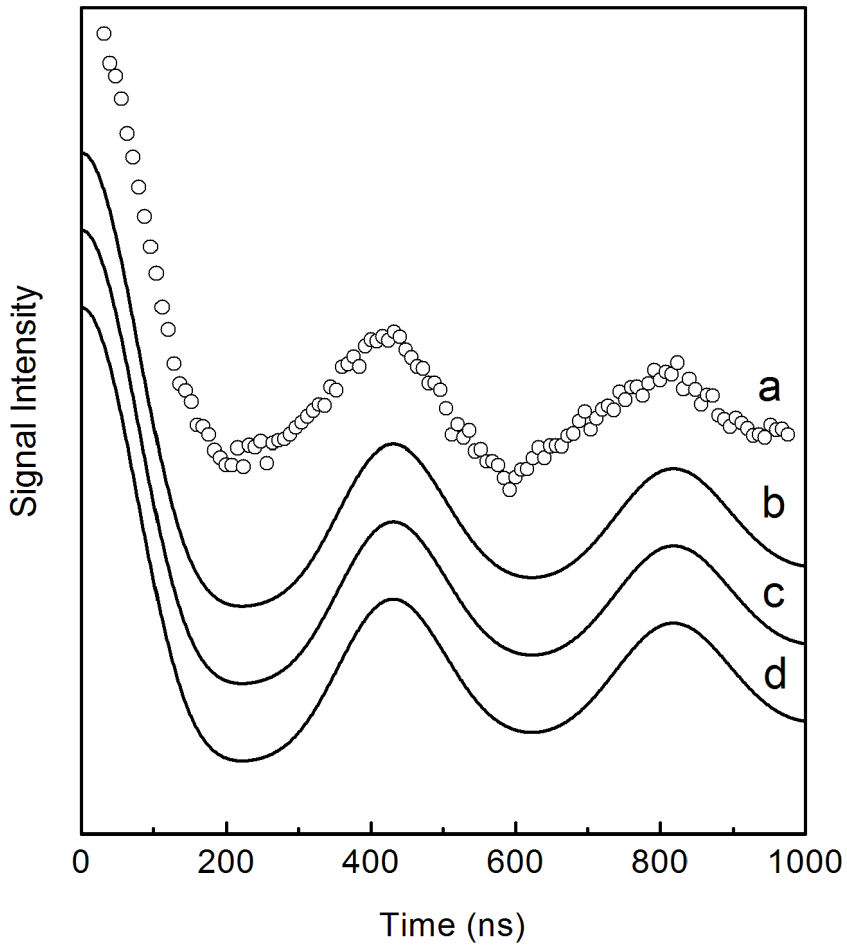

Figure I-10. (a) PELDOR signal of the interaction between $Y_D^{\bullet}$ and the S_2 state Mn cluster in PS II of *T. vulcanus* which is the same as the spectrum shown in Figure I-6. (B-D) Simulated PELDOR signals with the spin projections of (b) 1.77, -1.07, 1.09 and -0.75, (c) 1.39, -0.75, -1.05 and 1.01, and (d) 1.17, -0.77, -0.77 and 1.39 for Mn1-4, respectively. The combination patterns of the spin projections for (b-d) are corresponding to a2, a3 and d1, respectively.

Figure I-11

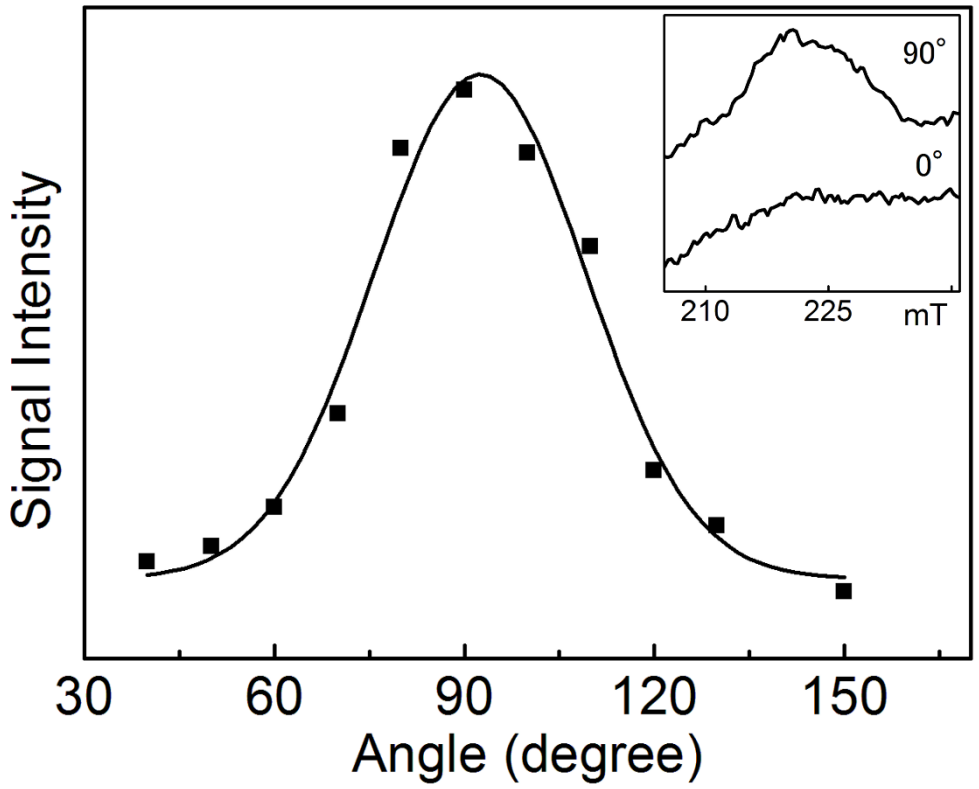

Figure I-11. Angular dependence between the CW EPR signals of the g_Z peaks of Cyt b559 in the oriented PS II membranes from spinach. The angle is defined between the membrane normal ***n*** of the samples and the extrinsic magnetic field $\boldsymbol{H_0}$. (Inset) CW-EPR spectra of the g_Z peaks at the angle θ = 0° and θ = 90°. Experimental conditions: microwave frequency, 9.44 GHz; microwave power, 201 μW; modulation amplitude, 0.8 mT; temperature, 5 K.

Figure I-12

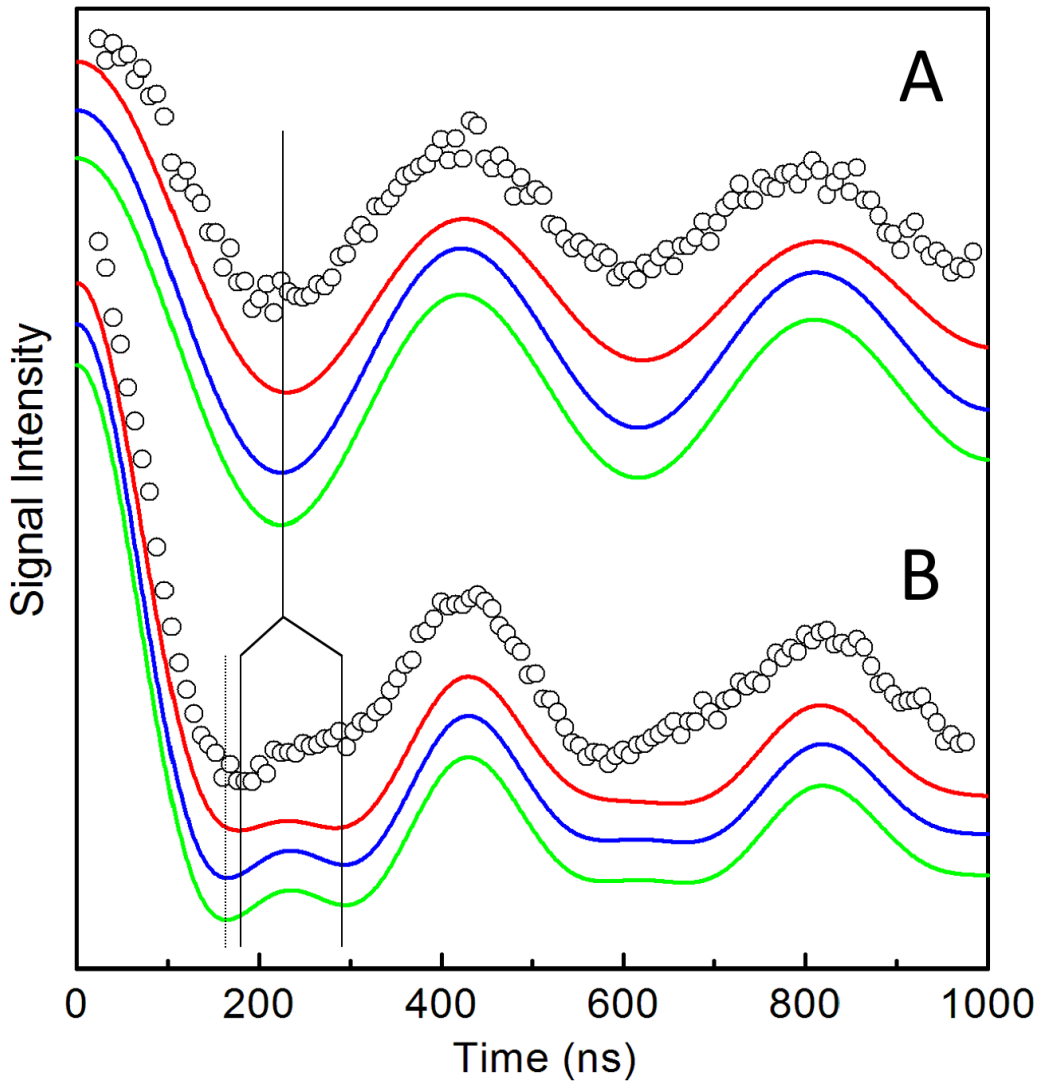

Figure I-12. (Circles) The experimental PELDOR spectra between $Y_D^{\bullet}$ and the Mn cluster in the S_2 state of the oriented PS II membranes, and (colored lines) the calculated spectra. The angle between the external magnetic field $\boldsymbol{H_0}$ and the membrane normal $\boldsymbol{n}$ was (A) θ = 0° or (B) θ = 90°. The spin projections of the calculated spectra for Mn1-4 were (red) 1.97, -1.2, 1.19 and -0.96 corresponding to the combination [++, -, +, -], (blue) 1.4, -0.66, -0.65 and 0.91 corresponding to [++, -, -, +], and (green) 1.22, -0.75, -0.7 and 1.23 corresponding to [+, -, -, ++], respectively. The vertical lines represent the first negative peak positions in the simulated spectra for (solid) the combination [++, -, +, -] and (dotted) the combinations [++, -, -, +] and [+, -, -, ++] (see text). Experimental conditions: observation microwave frequency, 9.61 GHz; pumping microwave frequency, 9.73 GHz; time interval, 1000 ns; magnetic field, 348 mT; repetition time, 2 ms; temperature, 5K.

Figure I-13

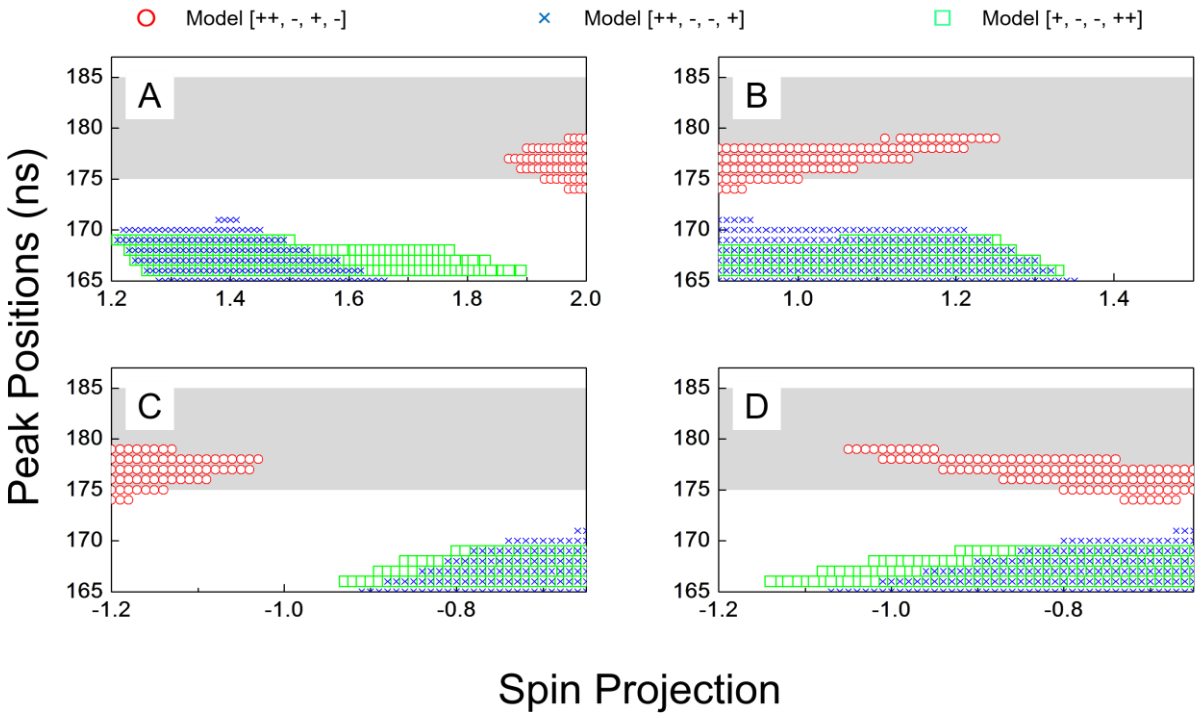

Figure I-13. The relation between the spin projections and the initial negative peak positions of the calculated PELDOR oscillation. Panels A shows the larger positive spin projection, and panel B shows the smaller positive spin projection. Panels C shows the negative spin projections of Mn2 for all the models, and panel D shows the negative spin projection for the other Mn ions (Mn3 for the models [++, -, -, +] and [+, -, -, ++], or Mn4 for the model [++, -, +, -]). Red circles, blue crosses and green squares represent the model [++, -, +, -], [++, -, -, +] and [+, -, -, ++], respectively. The gray part indicates the range of the peak positions by which the experimental oscillation is fitted within 5%.

Figure I-14

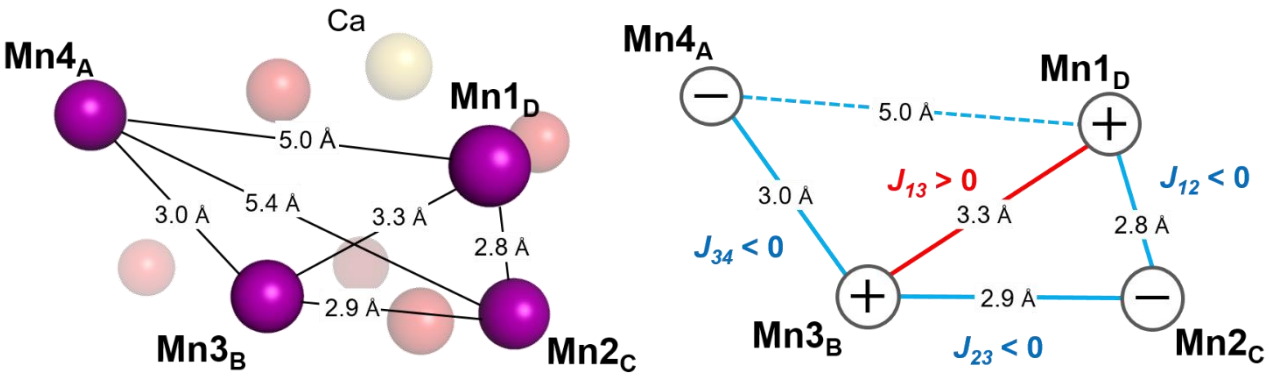

Figure I-14. (Left) Molecular structure of the Mn cluster and the distances between the Mn atoms based on the X-ray crystal structure. (Right) Model for the exchange couplings between Mn atoms in the S_2 state. The exchange couplings with the distance shorter than 5 Å are represented by the solid lines.

Table 1. Parameters of the spin projections of the Mn atoms estimated in previous reports.

Mn(III)	Mn(IV)	Mn(IV)	Mn(IV)	
1.70	1.27	-1.0	-0.99	Reference [24]
1.73	1.10	-1.04	-0.79	Reference [23]
1.73	1.12	-0.95	-0.90	Reference [29]
[a]1.39 ~ 1.89	[a] 0.99 ~ 1.34	[a] -1.11 ~ -0.82	[a] -1.02~ -0.75	Reference [29]

[a] The ranges of the spin projections obtained assuming A_{iso} is in the range of 165~225 MHz for a single Mn(III) and 187~253 MHz for a single Mn(IV) nuclei.

Table 2. Ranges of the spin projections estimated by fitting.

Mn1	Mn2	Mn3	Mn4	Combinations	Error range	
1.68 ~ 2.00	-1.20 ~ -0.65	0.90 ~ 1.50	-1.20 ~ -0.65	[++, -, +, -]	< 5%	
1.20 ~ 1.71	-1.09 ~ -0.65	-1.20 ~ -0.65	0.90 ~ 1.50	[++, -, -, +]	< 5%	Non-oriented PS II
0.90 ~ 1.50	-1.19 ~ -0.65	-1.20 ~ -0.65	1.20 ~ 2.00	[+, -, -, ++]	< 5%	
1.87~ 2.00	-1.20 ~ -1.03	0.90 ~ 1.25	-1.05 ~ -0.65	[++, -, +, -]	< 5%	
1.38 ~ 1.41	-0.66 ~ -0.65	-0.67 ~ -0.65	0.90 ~ 0.94	[++, -, -, +]	> 5%	Oriented PS II
1.06 ~ 1.25	-0.65 ~ -0.80	-0.92 ~ -0.65	1.21 ~ 1.50	[+, -, -, ++]	> 5%	

Chapter II

Position of the high-affinity Mn^{2+} site of photoactivation of OEC

Chapter Introduction

Assembly of PS II complex begins with formation of the core complex of D1/D2 and CP43/47 [46]. Then the oxygen evolving Mn cluster is constituted into D1 subunit of PS II precursor. In the assembly process of PS II, the extrinsic subunits PsbO, PsbU and PsbV (or PsbP and PsbQ) are suggested to bind to PS II core complex after the Mn cluster is formed.

Assembly of the Mn cluster is initiated by visible light in the presence of Mn and Ca ions. This process is called as “photoactivation”, which has been studied using OEC-removed PS II membranes. The photoactivation process was first reported by Cheniae and Martin in 1971 [47, 48]. In the early reports, the two-quantum mechanism was proposed for the model of photoactivation process [49, 50]. Thereafter many studies of the process have been described (reviewed in references [20, 46, 51, 52]). The photoactivation process requires two light-induced steps as described in Figure II-1. First, one Mn^{2+} ion binds to a cofactor-removed apo-PS II in the initial dark state, denoted as IM_0 [52]. The Mn^{2+} binding to apo-PS II is oxidized by illumination to Mn^{3+}, forming the next intermediate IM_1 state. Through the dark structural rearrangement, another Mn^{2+} binds in addition to Mn^{3+} in apo-PS II, and the IM_1* state is formed. Ca^{2+} is required to cause the rearrangement of OEC. It was indicated that binding of Ca^{2+} ion induces the subsequent photoactivation steps [53]. Further illumination helps to form the dimanganese intermediate Mn^{3+}-Mn^{3+} (IM_2 state), which has been monitored by XAS using partially heat-damaged PS II [54].

In the initial IM_0 state, there is one specific binding site of Mn^{2+} that is photo-oxidized to

Mn^{3+} [55]. Several researches reported about the high-affinity Mn^{2+} site in the IM_0 and IM_1 states. Site-directed mutagenesis studies reported that the mutation of D1-Asp170 inhibits the assembly of the Mn cluster except for Asp170Glu and Asp170His mutant [56]. The Mn^{3+} ions oxidized by freezing light, corresponding to the IM_1 state, was observed by parallel mode EPR [57]. The signals arising from Mn^{3+} were visible in the intact PS II; however, no such signal was observed in the site-directed Asp170Glu mutant. On the other hand, there is another report that Asp170His mutated PS II has active OEC [58], but the Mn^{3+} signal of Asp170His is different from the intact samples [57]. These reports demonstrated that Asp170 is essential for the initial assembly of the first binding Mn^{2+} ion, and Asp170 is close to the Mn^{2+} ion. However, it has remained unclear where the accurate location of the high-affinity Mn^{2+} site is.

In this section, we discuss the location of the high-affinity Mn^{2+} site within apo-PS II, inferred by the PELDOR measurement. It was indicated that the high-affinity site is located at the static position close to the native OEC structure. Comparison of the experiment data with the crystal structure gives the information as to the exact position of the high-affinity site.

Materials and Methods

Sample preparation

PS II membranes were isolated from market spinach as reported previously [35, 36].

To prepare the NaCl-treated apo-PS II samples, the membranes were suspended in a buffer which contains 400 mM sucrose, 20 mM Mes/NaOH, and 2 M NaCl (pH 6.5) at 1 mg of Chl/ml and were incubated for 20 min at 4 °C. Thereafter, the membranes were washed with a buffer containing 400 mM sucrose, 20 mM NaCl, 1 mM NH_2OH, and 20 mM Mes/NaOH (pH 6.5), and centrifuged at 35,000×g for 20 min [55]. After dark adaption at 4 °C for 1 min, 0.5 mM Na•EDTA was added. The samples were washed 3 times with a buffer containing 400 mM sucrose, 20 mM NaCl, and 40 mM Mes/NaOH (pH 6.5) denoted as the A-buffer in this article. Tris-treated apo-PS II was prepared by the PS II membranes incubating with a Tris/HCl buffer (pH 9.7) at 4 °C and then washing with the A-buffer for three times to exclude the cofactors.

The apo-PS II samples were illuminated for 1 min at 4 °C with room light to photo-oxidize Y_D. Then the indicated concentration of $MnCl_2$ and $CaCl_2$ was added. After centrifuging at 35,000×g for 20 min, the precipitate was moved to EPR tubes. The amount of Mn^{2+} bound to apo-PS II left in the supernatant was quantified by CW-EPR measurement [55].

For the preparation of the oriented membrane samples, concentrated spinach PS II was dried as described previously [59] and in Chapter I.

EPR measurements

CW-EPR measurements were recorded on a Bruker ESP-300E EPR spectrometer with a standard cavity (TE102). The amount of Mn^{2+} in the solution was measured by comparing with $MnCl_2$ solution contained in 50 µl capillary tubes at room temperature. Pulsed EPR and ELDOR were recorded on a Bruker E580 system with an Oxford Instruments liquid helium cryostat (CF935P, oxford GB). For the ESE field sweep measurement, a $\pi/2\text{-}\tau\text{-}\pi$ sequence was used with the time interval τ between the microwave pulses of 200 ns. A $\pi/2\text{-}\tau_1\text{-}\pi\text{-}\tau_1\text{-}\tau_2\text{-}\pi$ sequence with time interval τ_1 of 200 ns and τ_2 of 1400 ns was used for four-pulsed ELDOR (shown in Figure II-2), and a $\pi/2\text{-}\tau\text{-}\pi$ sequence with the time interval τ of 1400 ns was used for three-pulsed ELDOR [18, 59]. A microwave synthesizer (HP83751A, Hewlett-Packard) was utilized as the second microwave source [59].

PELDOR simulation methods

PELDOR spectra were simulated as described in Chapter I with few modifications. To calculate the PELDOR oscillation including the spin density distribution on $Y_D^{\bullet}$ and a Mn^{2+} atom, the dipole interaction *D* (eq. 12 in Chapter I) is rewritten as:

$$D = \sum_i \rho_i \frac{g_1 g_2 \beta^2}{h {R_i}^3} (1 - 3\cos^2 \Theta_i) \qquad (20)$$

where ρ_i is the spin density at the *i*-th (*i* = 1-7) carbon/oxygen atom of the $Y_D^{\bullet}$ molecule and R_i is the length between the *i*-th (*i* = 1-7) carbon/oxygen atom of the $Y_D^{\bullet}$ and the Mn^{2+} atom [41, 59]. Θ_i is the angle between the external magnetic field $\boldsymbol{H}$ and the distance vector $\boldsymbol{R_i}$. The coordinates of the related atoms were obtained from X-ray structure at the resolution of 1.95 Å (PDB: 4UB6).

Results

Quantification of Mn^{2+} binding to apo-PS II membranes

In the previous report, it was estimated that one Mn^{2+} ion binds to one apo-PS II at the concentration rates of PS II:Mn^{2+} = 1:4~12 in the presence of Ca^{2+} and PS II: Mn^{2+} = 1:1 in the absence of Ca^{2+} [55]. The lowest concentration where one Mn^{2+} binds to one PS II was applied in this study. Figure II-3 provides the CW-EPR results of which signals centered at *g* = 2 arises from the free Mn^{2+} ions. The NaCl-treated apo-PS II membranes of 1 mgChl/ml were suspended with the buffer containing 20 μM $MnCl_2$ (PS II:Mn^{2+} = 1:4) and concentrated by centrifugation. The amplitudes of the signals decreased by centrifugation, indicating that the Mn^{2+} binds to apo-PS II and free Mn^{2+} ions stay in the supernatant [55]. The amounts of Mn^{2+} ions in the buffer were count by the difference in a buffer containing $MnCl_2$ (black lines) and the supernatant after centrifugation of apo-PS II membranes (red lines). 1.4 and 0.4 Mn^{2+} ions bind to an apo-PS II in the absence and the presence of 10 mM Ca^{2+}, respectively. The amount of Mn^{2+} bound to apo-PS II was less in the presence of Ca^{2+}. The results corroborate that Ca^{2+} hinders Mn^{2+} binding to the non-specific sites and regulates Mn^{2+} binding to the high-affinity site [49, 55, 60, 61].

ESE-field swept spectra given in Figure II-4 were monitored with the pellet samples left after centrifugation which were washed in (a, d) the absence and (b, c) the presence of Ca^{2+} ions. The intensities of the signals were normalized with respect to the $Y_D^{\bullet}$ signal amplitude at *g* = 2. The broad signals with 60 mT width arises from Mn^{2+} concentrated with apo-PS II. The Mn^{2+} signal in the presence of Ca^{2+} is smaller than that in the absence of Ca^{2+}. This is consistent with that the number of Mn^{2+} ions bound to apo-PS

II count by CW-EPR measurement (Figure II-2). Dotted lines under both conditions (c, d) show the spectra after illumination for 3 min at 273 K. The Mn^{2+} signal disappeared after illumination in the absence of Ca^{2+}, indicating that multi-turnovers of the oxidation of Mn^{2+} occur.

PELDOR experiment with the non-oriented PS II membranes

In Figure II-5 (Panel A), (a) shows the PELDOR signals of the apo-PS II that was mixed at the concentration of 1 mgChl/ml with a buffer solution containing 20 μM Mn^{2+} in the absence of Ca^{2+}; the signals shown in (b) and (c) are recorded for the apo-PS II that were mixed in the presence of Ca^{2+} with (b) 40 μM Mn^{2+} and (c) 20 μM Mn^{2+}. For the PELDOR measurement the microwave frequencies were adjusted to excite the Mn^{2+} signals observed at 344 mT (blank arrow, Figure II-4) for observation pulses and the $Y_D^{\bullet}$ signal observed at 338 mT (filled arrow, Figure II-4) for pumping pulses. In order to reduce contribution of ESEEM beats, eight different signals recorded with varied τ_2 lengths (τ_2 = 1400-1456 ns with $\Delta\tau_2$ = 8 ns) were averaged [38, 62].

The signals in Figure II-5 (Panel B) were obtained after subtracting the linear baseline decay shown in panel A. The PELDOR oscillations measured in the absence of Ca^{2+} has the first negative peak at τ' = 296 ns and the first positive peak at τ' = 584 ns (Figure II-5Ba). Although the modulation depth of the signals was shallower, the period of the oscillations in the presence of Ca^{2+} was the same as that in the absence of Ca^{2+} (traces a and c in Figure II-4B), indicating that the oscillation does not arise from the non-specific Mn^{2+} binding sites. The second negative peak around τ' = 960 ns for 20 μM Mn^{2+} in the absence of Ca^{2+} (a) and for 40 μM Mn^{2+} in the presence of Ca^{2+} (b) could

result from baseline drift.

The distance between $Y_D^{\bullet}$ and the Mn^{2+} site was estimated to be 30.5 Å with the point dipole approximation. The distance distribution was evaluated to be 1.6 Å using the Deeranalysis 2011 program [63], implying that the Mn^{2+}-binding site is located in the immobile site. The PELDOR signal frequency was independent of the concentrations of Mn^{2+} (traces b and c). This indicates that the period of the PELDOR oscillation contributed from the non-specific Mn^{2+} binding site is longer than the recorded τ_2 lengths and the distance between $Y_D^{\bullet}$ and the non-specific Mn^{2+} binding sites is longer than 50 Å. The PELDOR modulation depth was deeper at low Mn^{2+} concentrations (traces b and c), which is consistent with that Ca^{2+} occupies the high-affinity Mn^{2+} site in that situation [60, 64, 65].

PELDOR experiment with the oriented PS II membranes

PELDOR results for the non-oriented PS II membranes provides the reliable information as to the position of Mn^{2+} site, which is on a sphere -like surface centered at Y_D aromatic ring [66]. PELDOR measurement using oriented samples can provides narrower possible area of Mn^{2+} binding site from the angular dependence of the interaction between the spin centers and the magnetic field [59].

Figure II-6 shows the PELDOR signals with the oriented apo-PS II sample in absence of Ca^{2+} ions. Panel B represent the subtraction of the linear background from panel A. Angular dependence of the signal peaks were detected. At the angle between the extrinsic magnetic field and the membrane normal θ is parallel (denoted as 0°), the

peaks of the oscillation were τ' = 292 ns for the 1st negative peak and τ' = 604 ns for the 1st positive peak. These peaks shifted to 220 and 582 ns for the 1st negative and positive peaks at the angle θ is 90°, when the angle between the membrane normal and the magnetic field was perpendicular. The oscillation includes a large contribution from long distances especially at the angle of 90°, which appears to be the non-specific Mn^{2+} binding sites located over 50 Å far from the $Y_D^{\bullet}$ center. The angular dependence of the oscillation pattern was pronounced at θ = 90°, because the angle between the magnetic field ***H*** and the distance vector ***R*** is regulated by the membrane orientation. The best fitting spectra are shown in Figure II-6B in red. The first negative peak at θ = 90° sensitively changed by the Mn^{2+} position, and the calculated oscillation of the provided narrower fitting parameters than that of the non-oriented samples as shown in Figure II-9B.

Effect on the high-affinity Mn^{2+} site caused by binding of PsbO

Through assembly process of PS II complex, it was suggested that PsbO binds after the Mn cluster is assembled into PS II [46], and it was revealed that PsbO binds near the Mn cluster and stabilizes the structure of OEC [4, 5]. In previous reports, both of the PS II samples whose extrinsic proteins PsbO, PsbP and PsbQ were removed and whose PsbP and PsbQ were removed but PsbO remains have been used for photoactivation studies. To clarify the effect of PsbO to the photoactivation process, we compared the PELDOR spectra of PS II with/without PsbO.

Figure II-7 shows the three-pulsed ELDOR results measured using (a) NaCl-treated and (b) Tris-treated apo-PS II membranes including 20 μM $MnCl_2$. PsbP and PsbQ were

removed from PS II membranes by NaCl-treatment, and PsbO, PsbP and PsbQ were depleted by Tris-treatment. The Tris-treated sample have very similar oscillation to the NaCl-treated sample, which indicates that the depletion of PsbO does not alter the location of the high-affinity Mn^{2+} site. Though PsbO is reported to interact with D1 and stabilize the Mn cluster, the result showed that PsbO does not affect to the structure of Mn^{2+} binding site at least the first step of the reconstitution process of the cluster.

Discussion

We reported the PELDOR oscillation arising from the interactions between Mn^{2+} bound to apo-PS II and $Y_D^{\bullet}$. The distance between $Y_D^{\bullet}$ and the Mn^{2+} site is estimated to be 30.5 Å with the assumption of the point dipole interaction, which is similar to the related location of $Y_D^{\bullet}$ and the Mn cluster in native OEC. The distance from the center of $Y_D^{\bullet}$ aromatic ring to the cofactors of OEC, Mn1, Mn2, Mn3, Mn4 and Ca, are 29.3, 32.0, 31.2, 30.2 and 30.7 Å, respectively [16, 17]. $Y_D^{\bullet}$ radical has the spin density distribution, which must be included for accurate calculation of the PELDOR signals [59]. Initially, we assumed that the Mn^{2+} affinity site is located within the OEC of the native PS II. Figure II-8 represents (a) the experimental and (b-f) the simulated PELDOR signals with the first positive peaks at (b) τ' = 526 ns for Mn1, (c) τ' = 580 ns for Mn4, (d) τ' = 610 ns for Ca, (e) τ' = 638 ns for Mn3 and (f) τ' = 686 ns for Mn2, respectively. The location of Mn4 is in good agreement with the PELDOR experimental results.

In Mn-depleted PS II, the amino-acid residues which ligate to the Mn or Ca atom in intact PS II cannot be arranged. If the Mn^{2+} has a monodentate coordination with a carboxylate, the distance distribution should be wider. The observed narrow distance distribution of the oscillation indicates that Mn^{2+} has a bidentate coordination to the surrounding carboxylates. Mn4 is the only location where two amino acids Asp170 and Glu333 ligate to a Mn atom in the native structure, so that Mn^{2+} can easily bind to the native position even under cofactor-depleted conditions.

The positions of the possible Mn^{2+} affinity site determined by fitting the PELDOR signals are located on the sphere-like curved surface whose center is the $Y_D^{\bullet}$ molecule. In

Figure II-9A, the gray curve represents the possible area of the high-affinity Mn^{2+} site. The gray points show where the calculated PELDOR oscillations have the first negative peaks at τ' = 290-320 ns and the first positive peaks at τ' = 575-595 ns.

The removal of the cofactors possibly causes structural changes around the OEC. If rotation of the carboxylate is considered, two Mn^{2+} sites are possible to have bidentate coordination with two ligand C=O in opposite side; one is the Mn4 site ligated between Asp170 and Glu333, and the other is the site between Glu189 and Ala344. The position between Glu189 and Ala344 is not the site for any cofactors in the native crystal structure, and the distance between these carboxylates is slightly long. Although Mn^{2+} ion might bind to the site between Glu189 and Ala344 if there is a structural modification, this is not consistent with the results of the site-directed mutant reported previously [56, 57].

The PELDOR signals obtained by the oriented PS II membranes provided precious fitting to the possible Mn^{2+} binding sites. Figure II-9B shows the points fitting to the oscillations both of the non-oriented and oriented PS II samples, where the simulated oscillations have the first negative peaks at τ' = 272-312 ns for θ = 0° and τ' = 200-240 ns for θ = 90° and the first positive peaks at τ' = 575-630 ns for θ = 0° and τ' = 560-615 ns for θ = 90° of the oriented PS II. The best fitting simulations are shown in Figure II-6B in red lines. Though the possible positions obtained from non-oriented PS II was sphere-like surface, the positions calculated by oriented membranes show the belt-like surface centered at the $Y_D^{\bullet}$. This result specifies the possible Mn sites. The gray area includes Mn4 site in the native structure, indicating that the position of Mn4 site is

the most suitable for the high-affinity Mn^{2+} site in the positions of the metal ions in the native OEC.

If the high-affinity Mn^{2+} site is located between Asp170 and Glu333, which is corresponding to the Mn4 place, the Mn^{2+}-connecting axis is fixed by the C=O orientations of the two carboxylates. The connection of the Mn^{2+} ion between Asp170 and Glu333 would form a partial prototype of the Mn cluster.

The first photoactivation step to IM_1 state proceeds by the photo-oxidation of the Mn^{2+} at the high-affinity site. The site-directed mutagenesis report demonstrated that Asp170Glu provides EPR invisible Mn^{3+} ion formed by light-induced oxidation of Mn^{2+}, indicating that Mn^{3+} is not located near Asp170Glu [57], and Asp170Glu mutation does not inhibit the formation of the O_2 active Mn cluster [56]. This could be explained by the length between C=O and the Mn ion, whose axial binding length of Mn^{3+} is longer than that of Mn^{2+}. If the high-affinity Mn^{2+} site is between Asp170 and Glu333, the shortened binding length between Asp170Glu and Glu333 might hinder the axial binding of Mn^{3+} and make the affinity weaker in IM_1 state. According to the photoactivation model proposed to date, the dark rearrangement process forming the IM_1* state requires long time (~70 sec) and have very low efficiency [67]. This mechanism gives an interpretation that the oxidized Mn^{3+} ion is released from the Mn^{2+} site, which shows the different EPR signal, therefore the Asp170Glu mutated PS II keeps high O_2 activity even though the mutation cannot keep Mn^{3+} affinity. Asp170His mutation also forms the O_2 active OEC, which does not affect the structure of the Mn cluster through the S state transitions [58]. Histidine residue has longer amino acid than aspartate residue,

and it might cause similar effect to Asp170Glu mutation in terms of the binding length to the Mn ion. We suggest that Glu333 as well as Asp170 supports binding of the Mn^{2+} ion and is essential for the first step of the photoactivation process.

In this study, we determined the position of the high-affinity Mn^{2+} site in photoactivation process of PS II utilizing the PELDOR distance measurement. It is suggested that the Mn^{2+} ion is located at the position corresponding to Mn4 in the native OEC, where the Mn^{2+} coordinate to Asp170 and Glu333. The structural information gave new insights into the IM_0 state and the forward process. This result would provide yet another clue about the mechanism of the photoactivation process.

Figures

Figure II-1

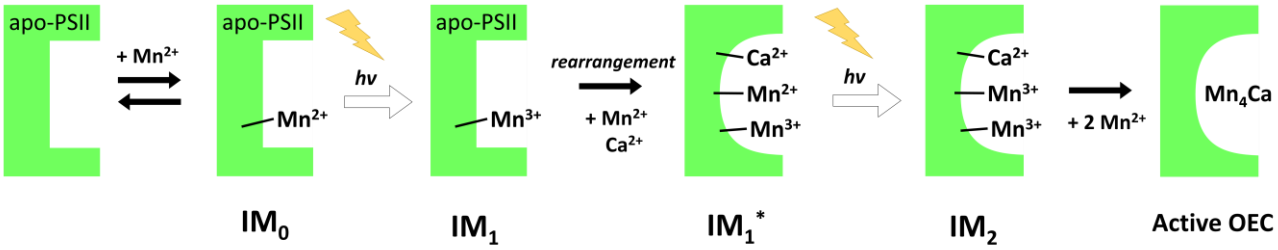

Figure II-1. The intermediates for the two-quantum photoactivation model of the Mn cluster.

Figure II-2

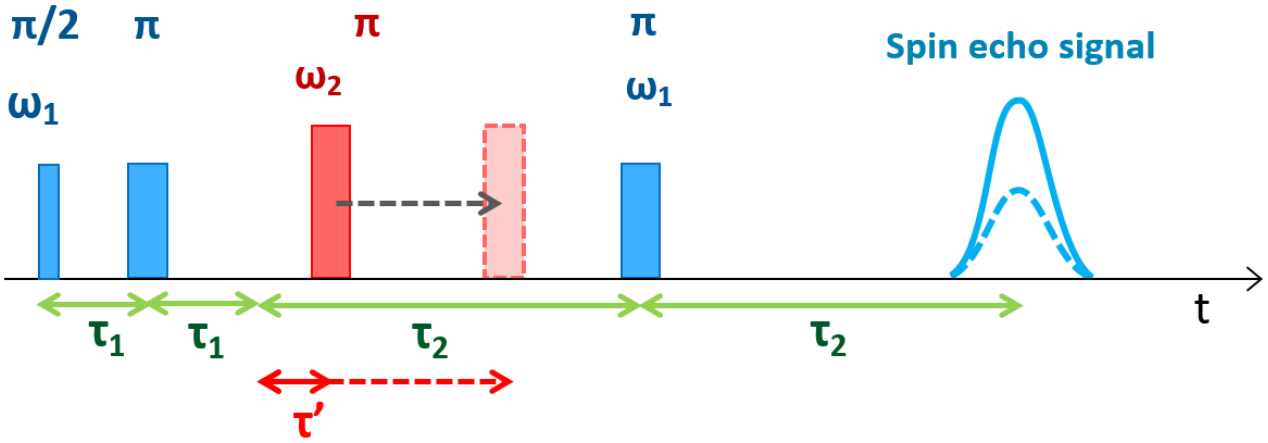

Figure II-2. Pulse sequence for the four-pulsed ELDOR measurement. The sequences of $\pi/2$-τ-π for 3-pulsed ELDOR and $\pi/2$-τ_1-π-τ_1+τ_2-π for the four-pulsed ELDOR were utilized.

Figure II-3

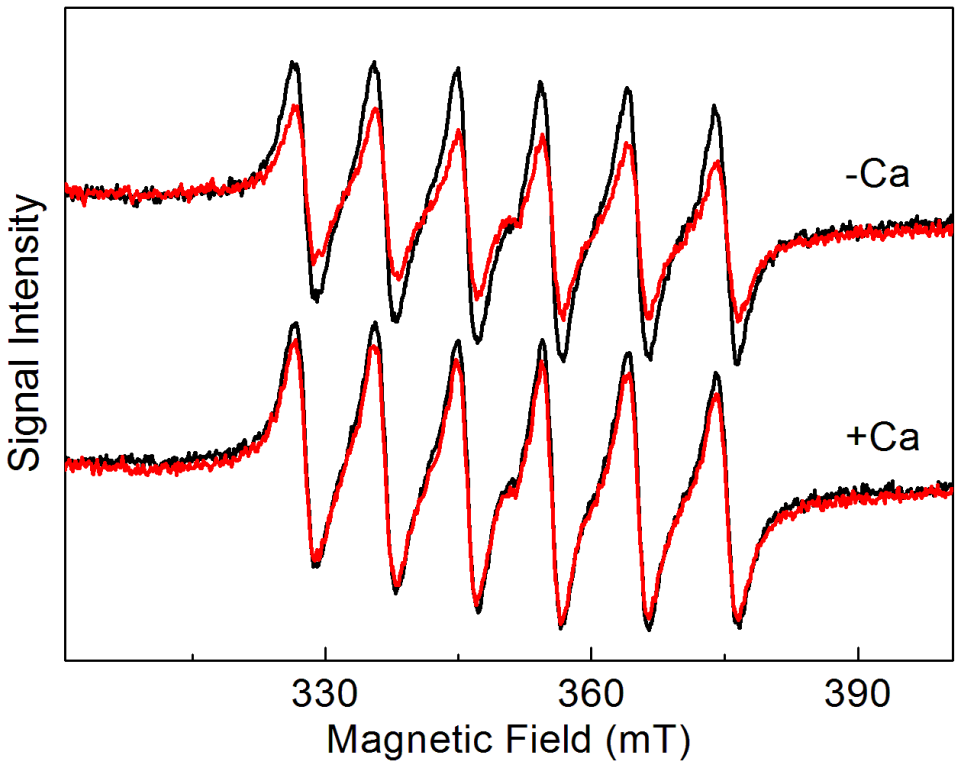

Figure II-3. CW-EPR field swept spectra of Mn^{2+} ions in the buffer containing 20 μM $MnCl_2$ (black lines) and the supernatant after centrifuging the mixture of the buffer and NaCl-treated apo-PS II at 1 mg of Chl/ml (red lines) in the absence (upper) and the presence (downer) of 10 mM Ca^{2+}. Experimental conditions: microwave frequency, 9.79 GHz; microwave power, 64 mW; field modulation amplitude, 0.8 mT at 100 kHz; time constant, 3 ms.

Figure II-4

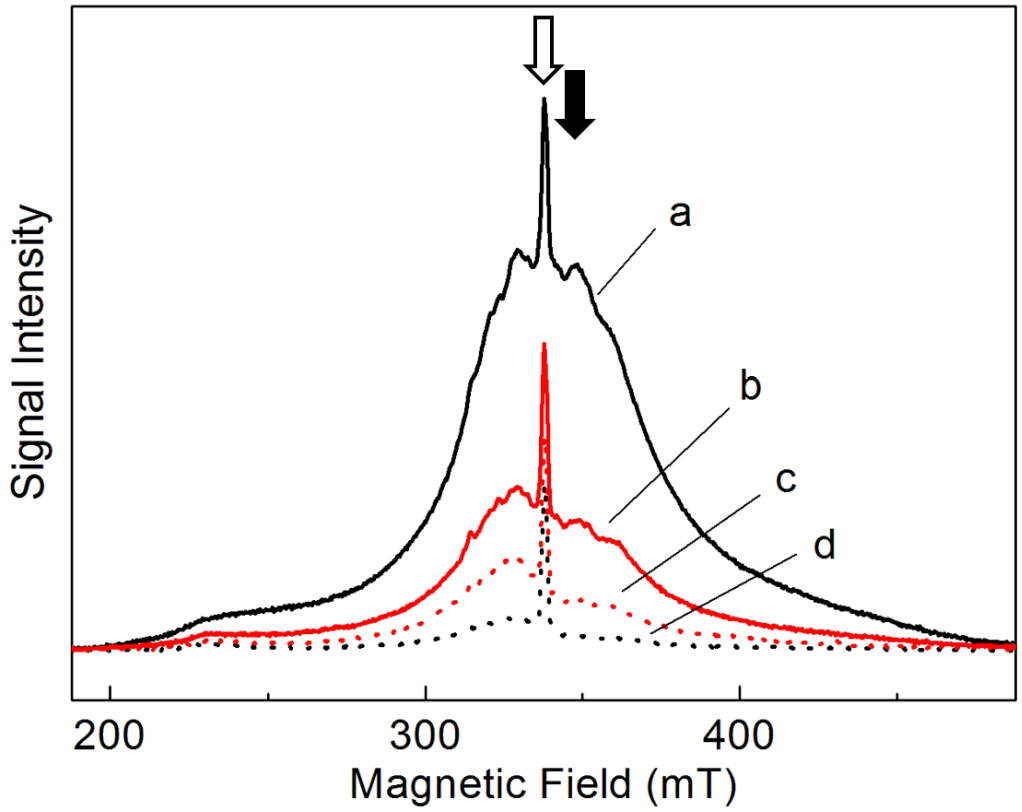

Figure II-4. ESE field swept spectra of the NaCl-treated apo-PS II in the absence (a, d) and the presence (b, c) of $CaCl_2$. The samples were in the dark state (a, b) and upon illumination for 3 min at 273 K, immediately frozen in a liquid N_2 bath (c, d). The signal intensities were normalized by the amplitude of $Y_D^{\bullet}$ at 344 mT. Experimental conditions: microwave frequency, 9.49 GHz; pulse length, 16 ns for $\pi/2$ pulses and 24 ns for π pulses; interval time τ between the microwave pulses, 200 ns; repetition time, 100 μs; temperature, 8 K. Arrows show the magnetic fields which is resonant for the observation (filled) and the pumping (blank) microwave frequencies in the PELDOR measurements.

Figure II-5

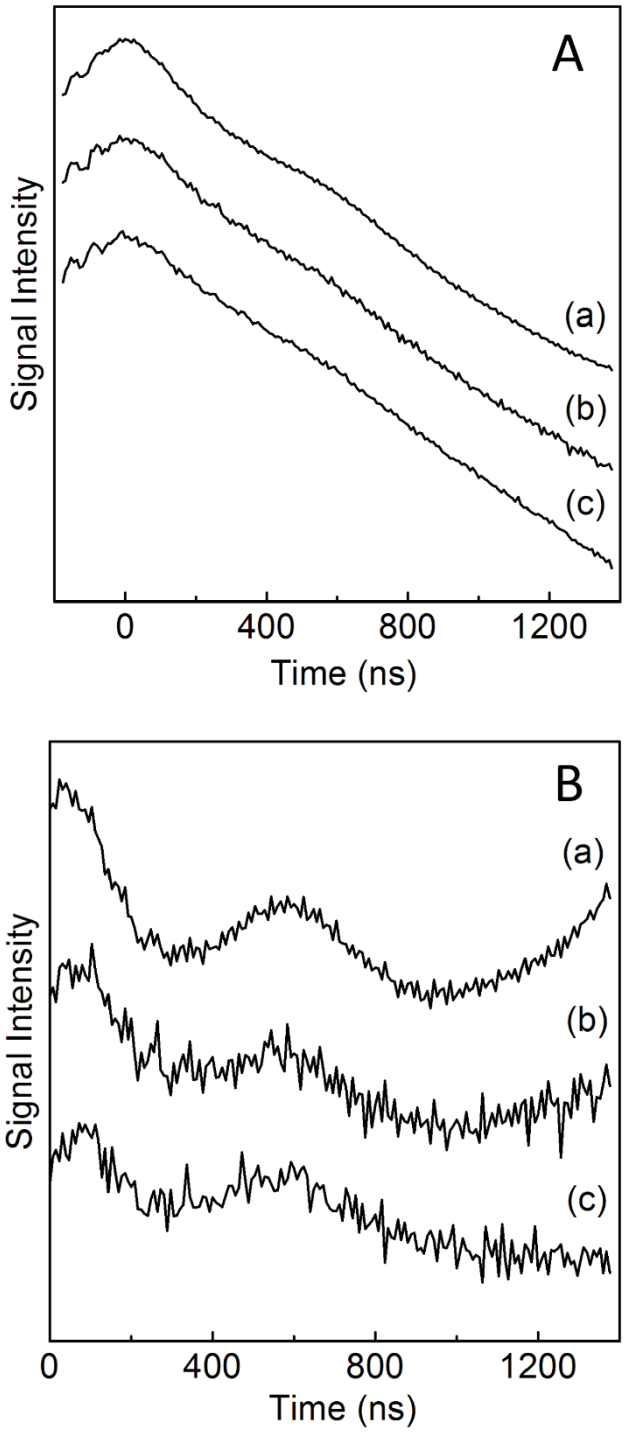
A
Signal Intensity
(a)
(b)
(c)
0
400
800
1200
Time (ns)
B
Signal Intensity
(a)
(b)
(c)
0
400
800
1200
Time (ns)

Figure II-5. Four-pulsed ELDOR spectra of the interaction between Mn^{2+} and $Y_D^{\bullet}$, obtained in 20 μM $MnCl_2$ (a, c) and 40 μM $MnCl_2$ (b) in the absence (a) and the presence (b, c) of $CaCl_2$. Panel B represents the signals after subtracting the linear decay background from the signals shown in panel A. Experimental conditions: microwave frequencies, 9.49 GHz for observation and 9.68 GHz for pumping pulses; pulse length, 16 and 24 ns for $\pi/2$ and π pulses; time interval between the first and the third pulses τ_2, 1400-1456 ns, the signals shown were summed up the PELDOR signals measured with the eight different time length in the range ($\Delta\tau_2$ = 8 ns); magnetic field, 350 mT; repetition time, 250 μs; temperature, 8 K.

Figure II-6

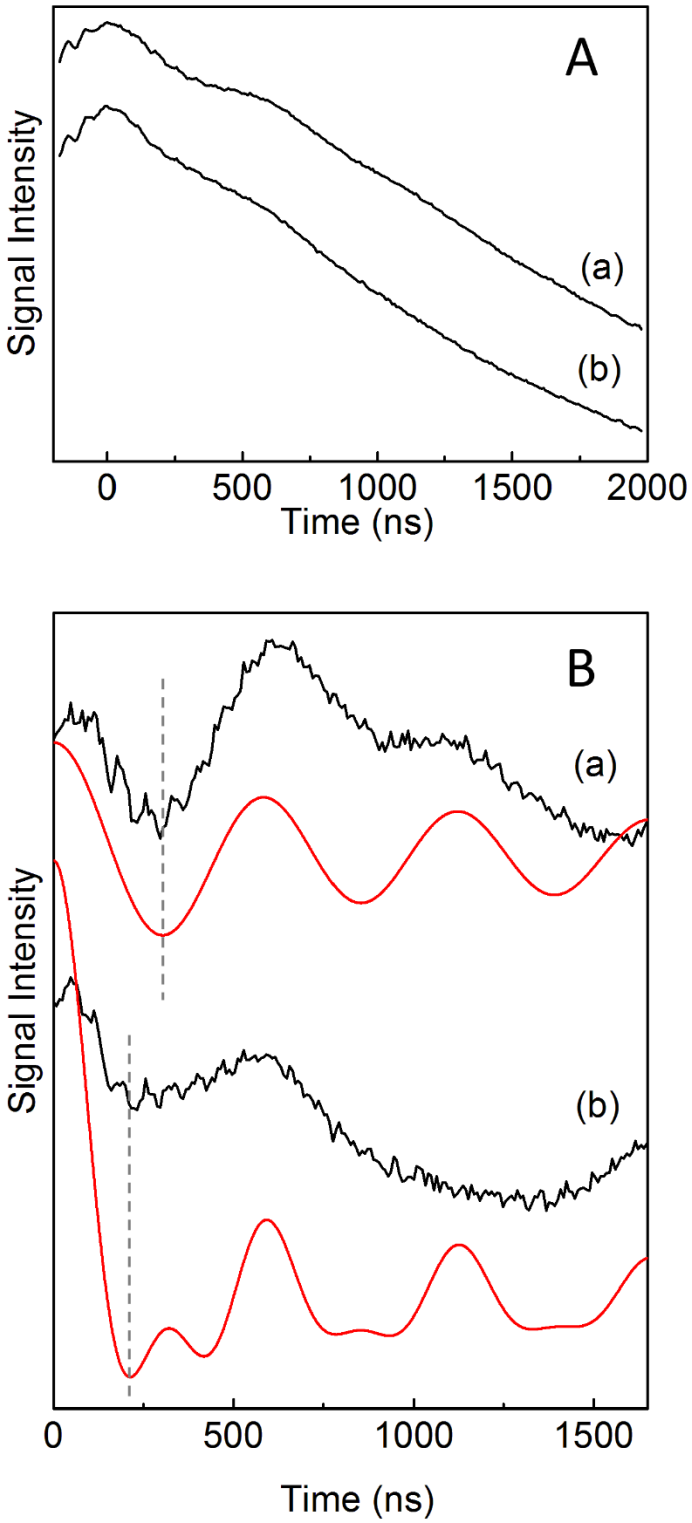
A
Signal Intensity
(a)
(b)
0
500
1000
1500
2000
Time (ns)
B
Signal Intensity
(a)
(b)
0
500
1000
1500
Time (ns)

Figure II-6. Four-pulsed ELDOR spectra of the interaction between Mn^{2+} and $Y_D^{\bullet}$ of the oriented apo-PS II membranes obtained in 20 μM $MnCl_2$ in the absence of $CaCl_2$. Panel B represents the signals after subtracting the linear decay background from the signals in panel A (black) and the simulated signals (red) using the best fitting coordinates of the possible Mn^{2+} site which is shown in Figure II-8. The angles between the external magnetic field $\boldsymbol{H_0}$ and the membrane normal $\boldsymbol{n}$ were $\theta = 0°$ (a) and $\theta = 90°$ (b), respectively. The broken lines show the best fitting position for the first negative peaks of the simulated spectra at $\tau' = 303$ ns for $\theta = 0°$ and $\tau' = 213$ ns for $\theta = 90°$. Experimental conditions: microwave frequencies, 9.69 GHz for observation and 9.489 GHz for pumping pulses; pulse length, 16 and 24 ns for $\pi/2$ and π pulses; time interval between the first and the third pulses τ_2, 1400-1456 ns, the signals shown were summed up the PELDOR signals measured with the eight different time length in the range ($\Delta\tau_2 = 8$ ns); magnetic field, 344.6 mT; repetition time, 250 μs; temperature, 8 K.

Figure II-7

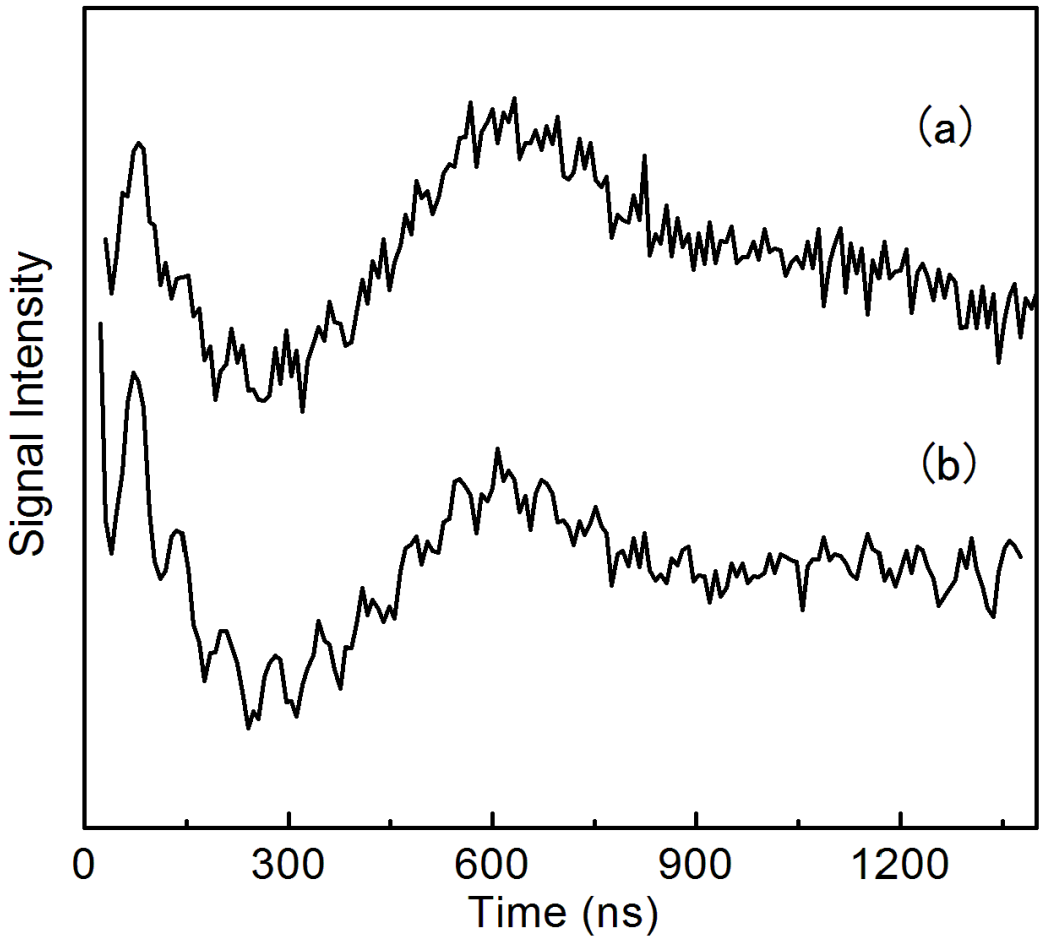

Figure II-7. Three-pulsed ELDOR spectra of NaCl-treated (a) and Tris-treated (b) apo-PS II samples with 20 μM $MnCl_2$. The signals were after subtracting the linear decay background. Experimental conditions: microwave frequencies, 9.52 GHz for observation and 9.80 GHz for pumping pulses; pulse length, 16 and 24 ns for $\pi/2$ and π pulses; time interval between the first and the third pulses τ, 1400-1480 ns, the signals shown were summed up the three time length in the range ($\Delta\tau_2$ = 40 ns); magnetic field, 348.6 mT; repetition time, 1000 μs; temperature, 8 K.

Figure II-8

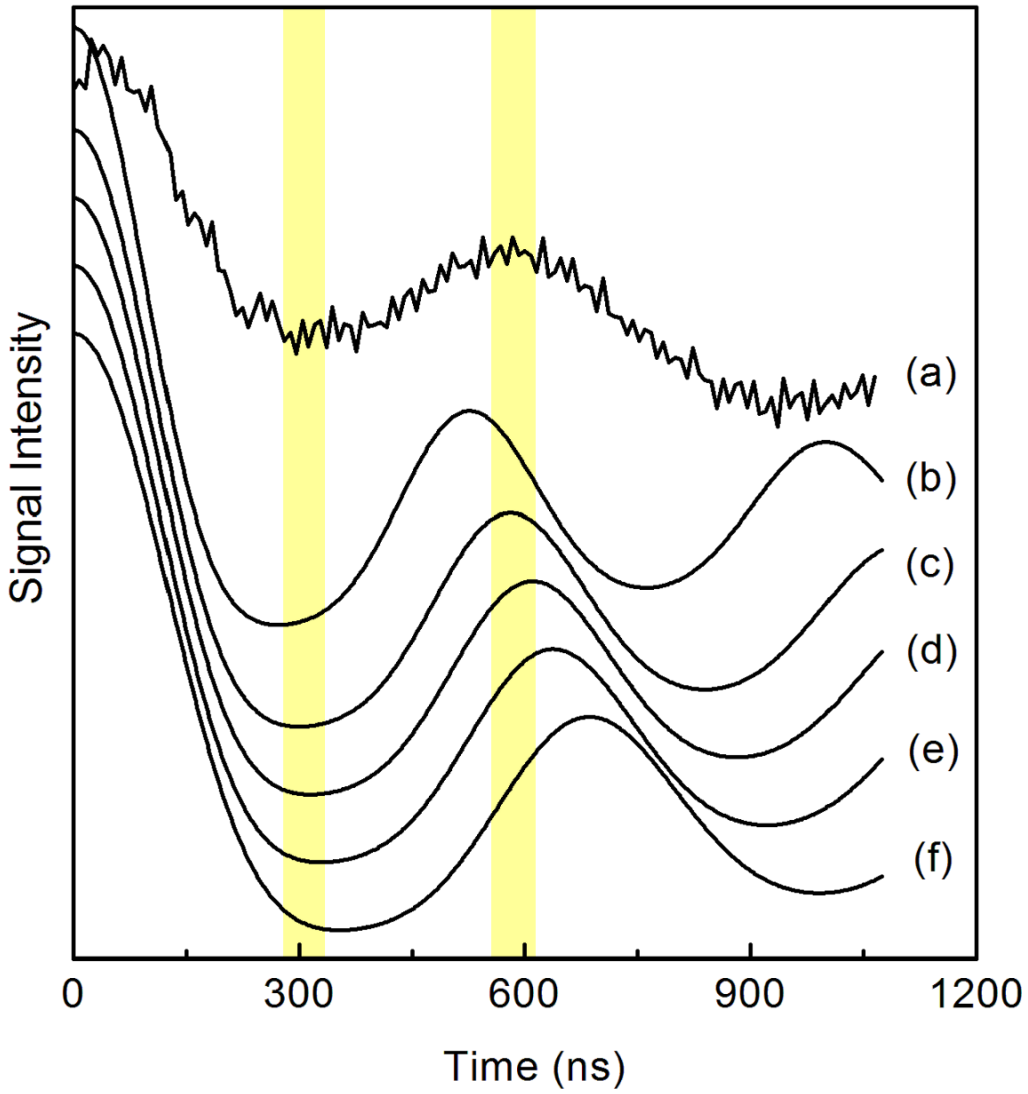

Figure II-8. PELDOR oscillations of the experimental (a) and the simulated (b-f) signals assuming that the Mn^{2+} is located on the cofactor sites in the native OEC. The trace a is the same to that shown in Figure II-4 B(a). The simulated signals are for Mn1 (b), Mn4 (c), Ca (d), Mn3 (e) and Mn2 (f) in the crystal structure represented in Figure G-4.

Figure II-9

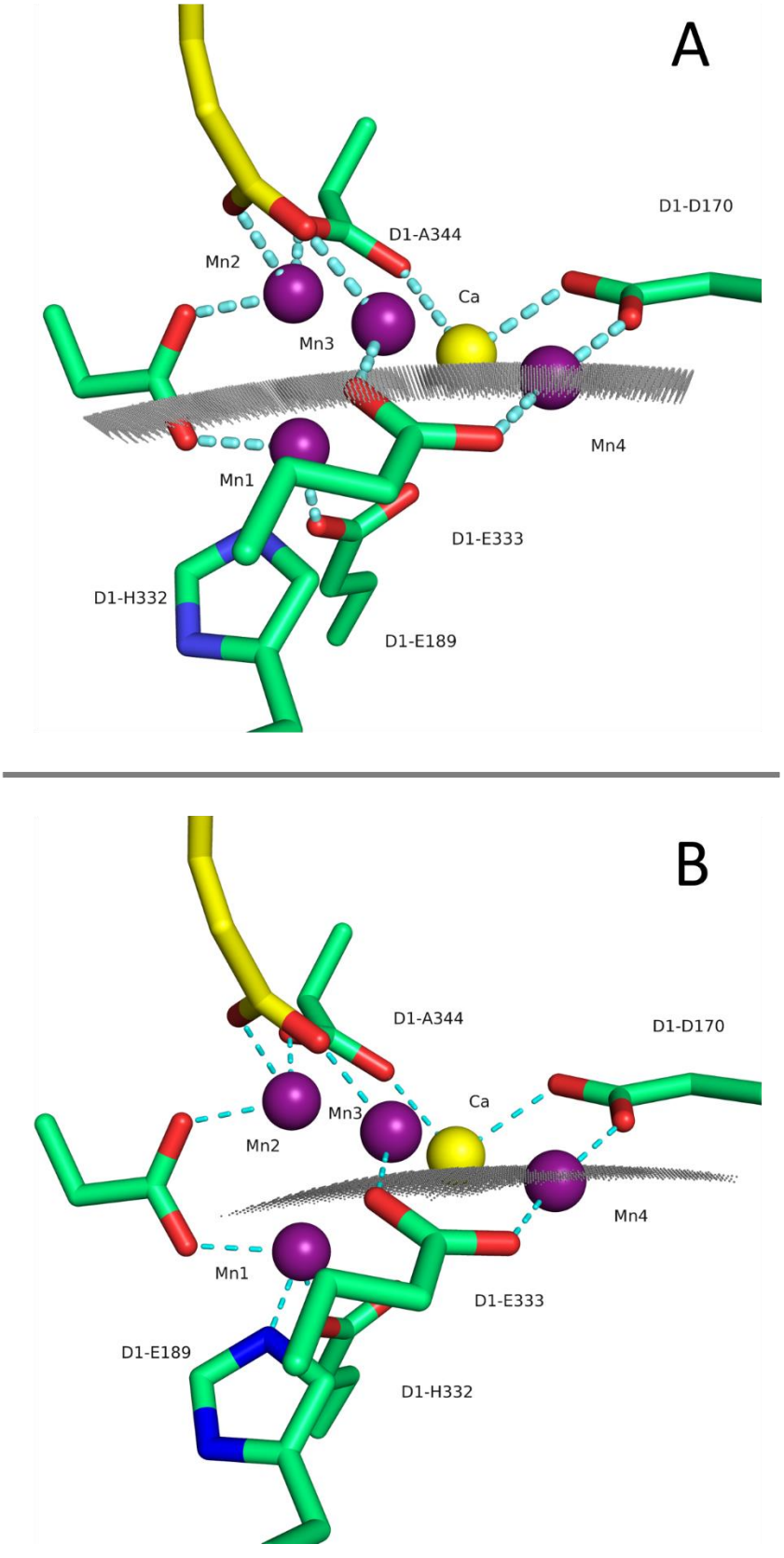
A
D1-D170
D1-A344
Mn2
Ca
Mn3
Mn4
Mn1
D1-E333
D1-H332
D1-E189
B
D1-A344
D1-D170
Mn3
Ca
Mn2
Mn4
Mn1
D1-E333
D1-E189
D1-H332

Figure II-9. The possible high-affinity Mn^{2+} sites. The gray dots represent the positions where the calculated PELDOR oscillations are corresponding to the experiment with (A) the non-oriented PS II and (B) both of the oriented and the non-oriented PS II. The simulation using the coordinates shown as gray dots were fitting to the experiments in terms of the first negative peaks at τ' = 290-320 ns and the first positive peaks at τ' = 575-595 ns for the non-oriented samples, and the first negative peaks at τ' = 272-312 ns for θ = 0° and τ' = 200-240 ns for θ = 90° and the first positive peaks at τ' = 575-630 ns for θ = 0° and τ' = 560-615 ns for θ = 90° of the oriented PS II.

References

[1] J.P. McEvoy, G.W. Brudvig, Water-splitting chemistry of photosystem II, *Chem. Rev.*, 106 (2006) 4455-4483.

[2] N. Nelson, C.F. Yocum, Structure and function of photosystems I and II, *Annu. Rev. Plant Biol.*, 57 (2006) 521-565.

[3] J. Messinger, G. Renger, Photosynthetic water-splitting in: G. Renger (Ed.) Promary processes of photosynthesis-part2: basic principles and apparatus, *Royal Society of Chemistry, Cambridge*, 2008, pp. 291-349.

[4] T.M. Bricker, J.L. Roose, R.D. Fagerlund, L.K. Frankel, J.J. Eaton-Rye, The extrinsic proteins of Photosystem II, *BBA-Bioenergetics,* 1817 (2012) 121-142.

[5] K. Ifuku, Localization and functional characterization of the extrinsic subunits of photosystem II: an update, *Biosci. Biotech. Bioch.*, 79 (2015) 1223-1231.

[6] K.N. Ferreira, T.M. Iverson, K. Maghlaoui, J. Barber, S. Iwata, Architecture of the photosynthetic oxygen-evolving center, *Science*, 303 (2004) 1831-1838.

[7] B. Loll, J. Kern, W. Saenger, A. Zouni, J. Biesiadka, Towards complete cofactor arrangement in the 3.0 Å resolution structure of photosystem II, *Nature,* 438 (2005) 1040-1044.

[8] A. Guskov, J. Kern, A. Gabdulkhakov, M. Broser, A. Zouni, W. Saenger, Cyanobacterial photosystem II at 2.9 Å resolution and the role of quinones, lipids, channels and chloride, *Nat Struct. Mol. Biol.*, 16 (2009) 334-342.

[9] V.K. Yachandra, K. Sauer, M.P. Klein, Manganese cluster in photosynthesis: Where plants oxidize water to dioxygen, *Chem. Rev*, 96 (1996) 2927-2950.

[10] J.H. Robblee, J. Messinger, R.M. Cinco, K.L. McFarlane, C. Fernandez, S.A. Pizarro, K. Sauer, V.K. Yachandra, The Mn cluster in the S_0 state of the oxygen-evolving

complex of photosystem II studied by EXAFS spectroscopy: Are there three di-m-oxo-bridged Mn_2 moieties in the tetranuclear Mn complex?, *J. Am. Chem. Soc*., 124 (2002) 7459-7471.

[11] J. Yano, J. Kern, K. Sauer, M.J. Latimer, Y. Pushkar, J. Biesiadka, B. Loll, W. Saenger, J. Messinger, A. Zouni, V.K. Yachandra, Where water is oxidized to dioxygen: Structure of the photosynthetic Mn_4Ca cluster, *Science*, 314 (2006) 821-825.

[12] R.M. Cinco, J.H. Robblee, J. Messinger, C. Fernandez, K.L.M. Holman, K. Sauer, V.K. Yachandra, Orientation of calcium in the Mn_4Ca cluster of the oxygen-evolving complex determined using polarized strontium EXAFS of photosystem II membranes, *Biochemistry*, 43 (2004) 13271-13282.

[13] Y. Pushkar, J. Yano, P. Glatzel, J. Messinger, A. Lewis, K. Sauer, U. Bergmann, V. Yachandra, Structure and orientation of the Mn_4Ca cluster in plant photosystem II membranes studied by polarized range-extended X-ray absorption spectroscopy, *J. Biol. Chem.*, 282 (2007) 7198-7208.

[14] J. Yano, V.K. Yachandra, Where water is oxidized to dioxygen: Structure of the photosynthetic Mn_4Ca cluster from X-ray spectroscopy, *Inorg. Chem*., 47 (2008) 1711-1726.

[15] K. Sauer, J. Yano, V.K. Yachandra, X-ray spectroscopy of the photosynthetic oxygen-evolving complex, *Coordin. Chem. Rev.*, 252 (2008) 318-335.

[16] Y. Umena, K. Kawakami, J.R. Shen, N. Kamiya, Crystal structure of oxygen-evolving photosystem II at a resolution of 1.9 Å, *Nature*, 473 (2011) 55-U65.

[17] M. Suga, F. Akita, K. Hirata, G. Ueno, H. Murakami, Y. Nakajima, T. Shimizu, K. Yamashita, M. Yamamoto, H. Ago, J.R. Shen, Native structure of photosystem II at 1.95 Å resolution viewed by femtosecond X-ray pulses, *Nature*, 517 (2015) 99-115.

[18] J.E. Banham, C.M. Baker, S. Ceola, I.J. Day, G.H. Grant, E.J.J. Groenen, C.T. Rodgers, G. Jeschke, C.R. Timmel, Distance measurements in the borderline region of applicability of CW EPR and DEER: A model study on a homologous series of spin-labelled peptides, J. *Magn. Reson.*, 191 (2008) 202-218.

[19] G.C. Dismukes, Y. Siderer, Intermediates of a Polynuclear Manganese Center Involved in Photosynthetic Oxidation of Water, P. Natl. *Acad. Sci.-Biol.,* 78 (1981) 274-278.

[20] D.J. Vinyard, G.M. Ananyev, G.C. Dismukes, Photosystem II: The Reaction Center of Oxygenic Photosynthesis, *Annu. Rev. Biochem.*, 82 (2013) 577-606.

[21] J. Messinger, J.H. Robblee, W.O. Yu, K. Sauer, V.K. Yachandra, M.P. Klein, The S_0 state of the oxygen-evolving complex in photosystem II is paramagnetic: Detection of EPR multiline signal, *J. Am. Chem. Soc.*, 119 (1997) 11349-11350.

[22] P. Geijer, S. Peterson, K.A. Ahrling, Z. Deak, S. Styring, Comparative studies of the S_0 and S_2 multiline electron paramagnetic resonance signals from the manganese cluster in Photosystem II, *BBA-Bioenergetics,* 1503 (2001) 83-95.

[23] L.V. Kulik, B. Epel, W. Lubitz, J. Messinger, ^{55}Mn pulse ENDOR at 34 GHz of the S_0 and S_2 states of the oxygen-evolving complex in photosystem II, *J. Am. Chem. Soc*., 127 (2005) 2392-2393.

[24] J.M. Peloquin, K.A. Campbell, D.W. Randall, M.A. Evanchik, V.L. Pecoraro, W.H. Armstrong, R.D. Britt, ^{55}Mn ENDOR of the S_2-state multiline EPR signal of photosystem II: Implications on the structure of the tetranuclear Mn cluster, *J. Am. Chem. Soc.*, 122 (2000) 10926-10942.

[25] L.V. Kulik, B. Epel, W. Lubitz, J. Messinger, Electronic structure of the Mn4OxCa cluster in the S_0 and S_2 states of the oxygen-evolving complex of photosystem II based

on pulse ^{55}Mn-ENDOR and EPR Spectroscopy, *J. Am. Chem. Soc.*, 129 (2007) 13421-13435.

[26] P.E.M. Siegbahn, A Structure-Consistent Mechanism for Dioxygen Formation in Photosystem II, *Chem.-Eur. J.*, 14 (2008) 8290-8302.

[27] P.E.M. Siegbahn, Structures and Energetics for O_2 Formation in Photosystem II, *Accounts. Chem. Res.*, 42 (2009) 1871-1880.

[28] P.E.M. Siegbahn, An Energetic Comparison of Different Models for the Oxygen Evolving Complex of Photosystem II, *J. Am. Chem. Soc.*, 131 (2009) 18238-+.

[29] N. Cox, L. Rapatskiy, J.H. Su, D.A. Pantazis, M. Sugiura, L. Kulik, P. Dorlet, A.W. Rutherford, F. Neese, A. Boussac, W. Lubitz, J. Messinger, Effect of Ca^{2+}/Sr^{2+} Substitution on the Electronic Structure of the Oxygen-Evolving Complex of Photosystem II: A Combined Multifrequency EPR, ^{55}Mn-ENDOR, and DFT Study of the S_2 State, *J. Am. Chem. Soc*., 133 (2011) 3635-3648.

[30] G.J. Yeagle, M.L. Gilchrist, R.M. McCarrick, R.D. Britt, Multifrequency pulsed electron paramagnetic resonance study of the S_2 state of the photosystem II manganese cluster, *Inorg Chem,* 47 (2008) 1803-1814.

[31] T.A. Stich, G.J. Yeagle, R.J. Service, R.J. Debus, R.D. Britt, Ligation of D1-His332 and D1-Asp170 to the Manganese Cluster of Photosystem II from Synechocystis Assessed by Multifrequency Pulse EPR Spectroscopy, *Biochemistry*, 50 (2011) 7390-7404.

[32] H. Hara, A. Kawamori, A.V. Astashkin, T. Ono, The distances from tyrosine D to redox-active components on the donor side of Photosystem II determined by pulsed electron-electron double resonance, *BBA-Bioenergetics*, 1276 (1996) 140-146.

[33] J.R. Shen, Y. Inoue, Binding and Functional-Properties of 2 New Extrinsic

Components, Cytochrome-C-550 and a 12-Kda Protein, in Cyanobacterial Photosystem-II, *Biochemistry*, 32 (1993) 1825-1832.

[34] J.R. Shen, N. Kamiya, Crystallization and the crystal properties of the oxygen-evolving photosystem II from Synechococcus vulcanus, *Biochemistry,* 39 (2000) 14739-14744.

[35] D.A. Berthold, G.T. Babcock, C.F. Yocum, A Highly Resolved, Oxygen-Evolving Photosystem-II Preparation from Spinach Thylakoid Membranes - Electron-Paramagnetic-Res and Electron-Transport Properties, *FEBS Lett.*, 134 (1981) 231-234.

[36] T. Ono, Y. Inoue, Effects of Removal and Reconstitution of the Extrinsic 33-Kda, 24-Kda and 16-Kda Proteins on Flash Oxygen Yield in Photosystem-II Particles, *BBA-Bioenergetics,* 850 (1986) 380-389.

[37] Y. Asada, R. Mutoh, M. Ishiura, H. Mino, Nonselective excitation of pulsed ELDOR using multi-frequency microwaves, *J. Magn. Reson*., 213 (2011) 200-205.

[38] G. Jeschke, DEER Distance Measurements on Proteins, *Annu. Rev. Phys. Chem*., 63 (2012) 419-446.

[39] C.W. Hoganson, G.T. Babcock, Protein Tyrosyl Radical Interactions in Photosystem-Ii Studied by Electron-Spin-Resonance and Electron Nuclear Double-Resonance Spectroscopy - Comparison with Ribonucleotide Reductase and Invitro Tyrosine, *Biochemistry*, 31 (1992) 11874-11880.

[40] H. Mino, A.V. Astashkin, A. Kawamori, An EPR and pulsed ENDOR study of the structure of tyrosine $Z^{\bullet}$ in Tris-treated photosystem II, *Spectrochim. Acta. A*, 53 (1997) 1465-1483.

[41] H. Nagai, Y. Fukushima, K. Okajima, M. Ikeuchi, H. Mino, Formation of Interacting

Spins on Flavosemiquinone and Tyrosine Radical in Photoreaction of a Blue Light Sensor BLUF Protein TePixD, *Biochemistry,* 47 (2008) 12574-12582.

[42] S. Kessen, C. Teutloff, J. Kern, A. Zouni, R. Bittl, High-Field ^{2}H-Mims-ENDOR Spectroscopy on PSII Single Crystals: Hydrogen Bonding of $Y_D^{\bullet}$, *Chemphyschem.,* 11 (2010) 1275-1282.

[43] M.F. Charlot, A. Boussac, G. Blondin, Towards a spin coupling model for the Mn-4 cluster in photosystem II, *BBA-Bioenergetics*, 1708 (2005) 120-132.

[44] D.A. Pantazis, M. Orio, T. Petrenko, S. Zein, W. Lubitz, J. Messinger, F. Neese, Structure of the oxygen-evolving complex of photosystem II: information on the S_2 state through quantum chemical calculation of its magnetic properties, *Phys. Chem. Chem. Phys.*, 11 (2009) 6788-6798.

[45] W. Ames, D.A. Pantazis, V. Krewald, N. Cox, J. Messinger, W. Lubitz, F. Neese, Theoretical Evaluation of Structural Models of the S_2 State in the Oxygen Evolving Complex of Photosystem II: Protonation States and Magnetic Interactions, *J. Am. Chem. Soc.*, 133 (2011) 19743-19757.

[46] K. Becker, K.U. Cormann, M.M. Nowaczyk, Assembly of the water-oxidizing complex in photosystem II, *J. Photoch. Photobio. B*, 104 (2011) 204-211.

[47] G.M. Cheniae, I.F. Martin, Effects of Hydroxylamine on Photosystem-II .1. Factors Affecting Decay of O2 Evolution, *Plant Physiol.*, 47 (1971) 568-&.

[48] G.M. Cheniae, I.F. Martin, Photoactivation of Manganese Catalyst of O_2 Evolution .1. Biochemical and Kinetic Aspects, *BBA-Bioenergetics,* 253 (1971) 167-181.

[49] N. Tamura, G. Cheniae, Photoactivation of the Water-Oxidizing Complex in Photosystem II Membranes Depleted of Mn and Extrinsic Proteins .1. Biochemical and Kinetic Characterization, *BBA-Bioenergetics*, 890 (1987) 179-194.

[50] A.F. Miller, G.W. Brudvig, Manganese and Calcium Requirements for Reconstitution of Oxygen-Evolution Activity in Manganese-Depleted Photosystem-II Membranes, *Biochemistry*, 28 (1989) 8181-8190.

[51] T. Ono, Metallo-radical hypothesis for photoassembly of $(Mn)_4$-cluster of photosynthetic oxygen evolving complex, *BBA-Bioenergetics*, 1503 (2001) 40-51.

[52] J. Dasgupta, G.M. Ananyev, G.C. Dismukes, Photoassembly of the water-oxidizing complex in photosystem II, *Coordin. Chem. Rev*., 252 (2008) 347-360.

[53] A.M. Tyryshkin, R.K. Watt, S.V. Baranov, J. Dasgupta, M.P. Hendrich, G.C. Dismukes, Spectroscopic evidence for Ca^{2+} involvement in the assembly of the Mn_4Ca cluster in the photosynthetic water-oxidizing complex, *Biochemistry*, 45 (2006) 12876-12889.

[54] M. Barra, M. Haumann, P. Loja, R. Krivanek, A. Grundmeier, H. Dau, Intermediates in assembly by photoactivation after thermally accelerated disassembly of the manganese complex of photosynthetic water oxidation, *Biochemistry*, 45 (2006) 14523-14532.

[55] T. Ono, H. Mino, Unique binding site for Mn^{2+} ion responsible for reducing an oxidized Y_Z tyrosine in manganese-depleted photosystem II membranes, *Biochemistry*, 38 (1999) 8778-8785.

[56] P.J. Nixon, B.A. Diner, Aspartate-170 of the Photosystem-II Reaction Center Polypeptide D1 Is Involved in the Assembly of the Oxygen-Evolving Manganese Cluster, *Biochemistry*, 31 (1992) 942-948.

[57] K.A. Campbell, D.A. Force, P.J. Nixon, F. Dole, B.A. Diner, R.D. Britt, Dual-mode EPR detects the initial intermediate in photoassembly of the photosystem II Mn cluster: The influence of amino acid residue 170 of the D1 polypeptide on Mn coordination, *J.*

Am. Chem. Soc., 122 (2000) 3754-3761.

[58] R.J. Debus, C. Aznar, K.A. Campbell, W. Gregor, B.A. Diner, R.D. Britt, Does aspartate 170 of the D1 polypeptide ligate the manganese cluster in photosystem II? An EPR and ESEEM study, *Biochemistry*, 42 (2003) 10600-10608.

[59] M. Asada, H. Nagashima, F.H.M. Koua, J.R. Shen, A. Kawamori, H. Mino, Electronic structure of S_2 state of the oxygen-evolving complex of photosystem II studied by PELDOR, *BBA-Bioenergetics,* 1827 (2013) 438-445.

[60] N. Tamura, G.M. Cheniae, Requirements for the Photoligation of Mn^{2+} in PS II Membranes and the Expression of Water-Oxidizing Activity of the Polynuclear Mn-Catalyst, *FEBS Lett.*, 200 (1986) 231-236.

[61] P.J. Booth, A.W. Rutherford, A. Boussac, Location of the calcium binding site in Photosystem II: A Mn2+ substitution study, *BBA-Bioenergetics*, 1277 (1996) 127-134.

[62] A.V. Astashkin, S.A. Dikanov, Y.D. Tsvetkov, Spectrometer Dead Time - Effect on Electron-Spin Echo Modulation Spectra in Disordered-Systems, Chem. *Phys. Lett.*, 136 (1987) 204-208.

[63] G. Jeschke, R.J.M. Abbott, S.M. Lea, C.R. Timmel, J.E. Banham, The characterization of weak protein-protein interactions: Evidence from DEER for the trimerization of a von Willebrand factor A domain in solution, *Angew Chem. Int. Edit.*, 45 (2006) 1058-1061.

[64] T.A. Ono, Y. Inoue, Reductant-Sensitive Intermediates Involved in Multi-Quantum Process of Photoactivation of Latent O_2 Evolving System, *Plant Cell Physiol*., 28 (1987) 1293-1299.

[65] L. Zaltsman, G.M. Ananyev, E. Bruntrager, G.C. Dismukes, Quantitative kinetic model for photoassembly of the photosynthetic water oxidase from its inorganic

constituents: Requirements for manganese and calcium in the kinetically resolved steps, *Biochemistry*, 36 (1997) 8914-8922.

[66] M. Asada, H. Mino, Location of the High-Affinity Mn^{2+} Site in Photosystem II Detected by PELDOR, *J. Phys. Chem. B*, 119 (2015) 10139-10144.

[67] D.R.J. Kolling, N. Cox, G.M. Ananyev, R.J. Pace, G.C. Dismukes, What Are the Oxidation States of Manganese Required To Catalyze Photosynthetic Water Oxidation?, *Biophys. J.*, 103 (2012) 313-322.

Acknowledgement

I appreciate Prof. Hiroyuki Mino for his leadings, helpful advices, technical support and kind encouragement. I also appreciate to Prof. Takumi Noguchi for helpful advices and discussions. I greatly thank to Prof. Jian-Ren Shen in Okayama University for sample preparations of *T. vulcanus* PS II and significant advices. I am grateful to Prof. Christopher W. M. Kay for kind technical suggestions on PELDOR measurement. I also thank to Dr. Yuki Kato and Dr. Ryo Nagao and all members in photo-bioenergetics laboratory for helpful discussions and kind support. This research was supported by Program for Leading Graduate Schools" Integrative Graduate Education and Research in Green Natural Sciences" from the Ministry of Education, Culture, Sports, Science and Technology of Japan (MEXT), and Research Fellowship of the Japan Society for the Promotion of Science (JSPS) for Young Scientists.